INFORMATION TO USERS

This manuscript has been reproduced from the microfilm master. UMI films the text directly from the original or copy submitted. Thus, some thesis and dissertation copies are in typewriter face, while others may be from any type of computer printer.

The quality of this reproduction is dependent upon the quality of the copy submitted. Broken or indistinct print, colored or poor quality illustrations and photographs, print bleedthrough, substandard margins, and improper alignment can adversely affect reproduction.

In the unlikely event that the author did not send UMI a complete manuscript and there are missing pages, these will be noted. Also, if unauthorized copyright material had to be removed, a note will indicate the deletion.

Oversize materials (e.g., maps, drawings, charts) are reproduced by sectioning the original, beginning at the upper left-hand corner and continuing from left to right in equal sections with small overlaps.

Photographs included in the original manuscript have been reproduced xerographically in this copy. Higher quality 6" x 9" black and white photographic prints are available for any photographs or illustrations appearing in this copy for an additional charge. Contact UMI directly to order.

ProQuest Information and Learning
300 North Zeeb Road, Ann Arbor, MI 48106-1346 USA
800-521-0600

INVESTIGATION INTO THE STATIC AND FATIGUE BEHAVIOUR OF A HELICOPTER MAIN ROTOR YOKE MADE OF COMPOSITE MATERIALS

By

Stéphanie Lalonde

Department of Mechanical Engineering

McGill University, Montréal

January 2000

A thesis submitted to the Faculty of Graduate Studies and Research in partial fulfilment of the requirements of the degree of Master of Engineering

Abstract

The Bell Helicopter M407 main rotor yoke is a structural helicopter part made of laminated glass-epoxy composite material. Delamination failure of the main rotor yoke under static and fatigue loading conditions is investigated, both analytically and experimentally. A finite element model of the yoke is developed with a commercial finite element code, using the 'dummy plies' technique to allow modeling of a tapered laminate. The model is validated against the available experimental data. A set of static and fatigue experiments – limited to beamwise bending loads – are performed on representative test specimens cut out of actual yokes. The model is able to accurately predict the location of initial static failure, which corresponds to the interlaminar shear stress concentration predicted by the stress analysis. Results of the specimen fatigue tests are successfully correlated with the glass-epoxy material fatigue properties, using the Normalized Fatigue Life Model and the finite element model of the specimen.

Résumé

La chape du rotor principal de l'hélicoptère Bell 407 est une pièce structurale faite de matériaux composites fibre de verre / époxy. Cette thèse présente une étude analytique et expérimentale de la rupture par délamination de la chape du rotor principal sous des conditions de chargement statiques et en fatigue. Un modèle de la chape est développé à l'aide d'un logiciel commercial d'éléments finis, utilisant la technique de *réduction des plis* pour faciliter la modélisation d'un laminé à épaisseur variable. Ce modèle est validé par le biais de résultats expérimentaux. Une série d'essais statiques et en fatigue – limités à des chargements en flexion longitudinale – est effectuée sur des spécimens représentatifs obtenus à partir de chapes. Le modèle est capable de prédire avec précision l'emplacement de la rupture initiale sous un chargement statique; celui-ci correspond à l'emplacement où les contraintes maximales en cisaillement interlaminaire sont prédites par l'analyse de contraintes. Une corrélation entre les résultats des essais en fatigue et les propriétés en fatigue des matériaux fibre de verre / époxy est établie avec succès, à l'aide du modèle éléments finis du spécimen et du *Modèle normalisé de durée de vie en fatigue*.

Acknowledgements

I would first like to thank my supervisor Prof. Larry Lessard for his guidance and support during the course of this research. I would also like to thank to Wafaa Ishak and Dorina Mihail at Bell Helicopter for their advice and help; it was greatly appreciated. Thanks also to Mark Hollingworth at the McGill Office of Liaison with Industry for his help in making this project happen.

I would also like to thank Jean-Louis Fernandes at the Bell Helicopter tooling department, and Gary Savard at the McGill Mechanical engineering lab, for their precious help with the experimental part of this research.

Thanks must go to my colleagues in the computer lab at 550 Sherbrooke, especially to Pål Aasrum and Marta Slanik, for their friendship and encouragement. And thank you especially, Remo, for your patience and understanding throughout the course of this project. I know it has not been easy.

Finally, I would like to acknowledge and thank the Natural Sciences and Engineering Research Council for its financial support.

Table of Contents

List of Figures

List of Tables

1 Introduction

1.1 Motivation

In recent years, composite materials have been used extensively in helicopter dynamic structures, initially for blade construction, and more recently in other highly loaded dynamic parts. The introduction of composites in highly loaded structures has resulted in major performance improvements. Besides their superior strength-to-weight ratio, composites also provide unique design capabilities to tailor the material properties for specific requirements, such as strength, stiffness or dynamic characteristics.

Recently, an increasing number of helicopter rotor hubs have been built of composite materials. These new hub designs exhibit significant advantages over conventional articulated rotors: lower weight, better corrosion resistance, reduced number of parts, low maintenance costs and better damage tolerance capabilities. The Bell 407 main rotor hub (Figure 1) is one such new design. Its primary load bearing part, the main rotor yoke, is a four-bladed single piece structure made of glass-epoxy composite. The yoke carries the blades' centrifugal force, while the tapered flexure allows elastic bending of the part to accommodate the blades cyclic flapping motion. The main rotor yoke is thus subjected to a complex dynamic loading environment: low-cycle axial centrifugal force, and high-cycle beamwise and chordwise bending moments.

Currently, the long-term behavior of composite structural components subjected to dynamic loads is mainly addressed through testing programs, which are both long and costly. Moreover, the analytical methods used are rather empirical, relying heavily on specific laboratory data. Therefore, with the increasing number of structural applications of composite materials, where a critical part is subjected to a complex dynamic load environment, there is a strong need to develop reliable analytical tools to predict their fatigue behavior and damage tolerance capabilities.

The present study is aimed at developing a methodology which will allow to predict the delamination failure of a complex laminated composite structure under fatigue loading conditions. This research work will concentrate on the Bell M407 Main rotor yoke.

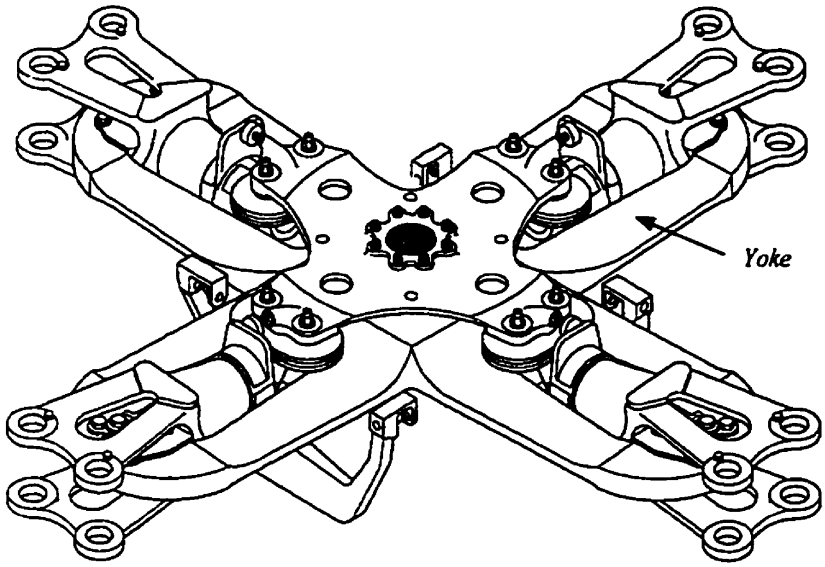

Figure 1 – The 407 main rotor hub

1.2 Literature review

Delamination is a primary mode of failure of laminated composites, and has been of interest since the earliest developments of composite structures. There are two basic approaches to predict the delamination strength of laminated composites. The mechanics of materials approach [1-24] uses stress-based failure criteria to predict delamination, comparing the material strength properties to the local stress field in the laminate. The second approach uses fracture mechanics techniques [25-30] to predict delamination failure. A review is presented of both methods. However, much more emphasis is given on the mechanics of materials approach as this is the method that will be used in the present study.

Delamination is a three-dimensional mode of failure, and is primarily caused by interlaminar stresses. Considerable work has been done to characterize the interlaminar stress state in laminates under axial tension. A good review of the subject is presented in [1]. The free edge delamination problem has also been extensively studied by many authors. In an early work [2], Pipes and Pagano used a finite-difference solution to determine the three-dimensional stress state in a laminated composite. Their results provided an explanation of the mechanisms responsible for edge delamination, showing that in the area near a free edge, there is a rise in the interlaminar stresses due to the mismatch of the elastic properties between the plies. Thus the Classical Lamination Theory, which assumes a state of plane stress, is no longer valid near a free edge, and more detailed analysis methods are required to determine this full three-dimensional state of stress.

Wang and Crossman [3] developed a simple two-dimensional finite element method, which can be used to study the free edge problem. The so-called quasi-three-dimensional finite element method is capable of determining the three-dimensional state of stress in symmetrical laminates under uniaxial tension, while avoiding the complexity and computational cost of a full three-dimensional finite element analysis. Raju and Crews [4] used the same approach, but with 8-noded isoparametric quadrilateral elements instead of 3-noded triangular elements near the free edge.

On the same problem, Kim and Soni [5, 6] used the global-local mathematical model developed by Pagano and Soni [7], to calculate the interlaminar stress distribution near the free-edge. They first studied separately the influence of the interlaminar normal stress [5] and the interlaminar shear stresses [6] on the delamination strength of various laminates. To overcome the problems caused by stress singularities near the free edge, a stress averaging method, similar to the approach developed by Whitney and Nuismer [8] for notched laminates, was used together with the maximum stress criterion. Predictions of delamination onset showed good correlation with the experimental results, except for those laminates for which both the normal and shear interlaminar stresses were important. It was therefore concluded that there is an interaction between the normal and shear

interlaminar stresses, and that failure prediction should take both stresses into account. Therefore, using the same method of analysis, they conducted a study [9] on a new set of laminates providing various ratios of interlaminar normal stress and shear stress at the interface of interest. Failure was predicted using a tensor polynomial delamination failure criterion, which was developed based on the Tsai-Wu failure criterion. A reasonable agreement was found between the analytical predictions and the experimental results.

Brewer and Lagace [10] used a similar quadratic stress criterion, along with the average stress method, to predict delamination at the free-edge. The out-of-plane stresses at free edges were estimated using the solution method proposed by Kassapoglou and Lagace [11], based on overall force and moment equilibrium and the principle of minimum complementary energy. Strength prediction correlated reasonably both with the experimental data and with data previously reported in literature.

Fish and Lee [12] studied the delamination onset strength of symmetric composite laminates under tension, based on the failure of a thin interply resin layer. Interlaminar stress values were obtained using a quasi-three-dimensional finite element model. Delamination failure, predicted by the same failure criterion used in [9] and the average stress method, was in good agreement with the experimental results. The calculated values of interlaminar shear stress showed to be sensitive to the finite element mesh size, while the interlaminar normal stress was insensitive to it.

Fracture mechanics techniques, concerned with failure of materials by crack initiation and propagation, are widely used for failure analysis of common isotropic materials such as metals. Since the early applications of composite materials, designers and researchers have looked into possibilities to adapt these methods to predict delamination of composite laminates. The most widespread approach uses the local strain energy release rate to characterize the delamination initiation and growth. A good review of the method is presented in [13].

Most of the prior work done on delamination failure of composites was exclusively focused on symmetric laminates under uniaxial extension. A few studies however, considered general loading conditions, and modified previous analysis tools. Armanios and Rehfield [14] used a sublaminate modeling approach to determine the interlaminar stresses and strain energy release rates in composite laminates under bending and combined bending and extension. The shear deformation theory used to derive the closed-form solution provides a good estimate of the interlaminar stresses, but is inaccurate for normal interlaminar stresses. Chan and Ochoa [15] derived a quasi-three-dimensional finite element formulation for the analysis of general composite laminates under combined loading conditions. The model allows to determine the interlaminar normal and shear stress distributions, as well as strain energy release rates, for composite laminates subjected to tension, bending and torsion loads. Fish [16] adapted the finite element formulation of Chan and Ochoa to perform the stress analysis of composite beam rotor components, subjected to axial tension, torsion and both beamwise and chordwise bending loads. No failure analysis was performed based on the calculated stresses.

The tapered geometry of the yoke is achieved by gradually dropping internal plies along the flexure. However, these ply drop-offs introduce geometrical and material discontinuities in the structure, resulting in local stress concentrations which may lead to delamination. In the last 15 years, several studies have been conducted on the failure mechanisms of tapered laminates. Many of these studies were directly motivated by applications in composite rotor hub flexures, either at Bell Helicopter Textron, McDonnell Douglas Helicopters or Westland Helicopters.

Kemp and Johnson [17] used a two-dimensional finite element analysis to determine the stress state at the drop-off location in quasi-isotropic laminates containing up to three dropped plies, under axial tension or compression loads. The maximum stress criterion was used to predict the failure of the pure resin region around the ply drop-off. However, no experiments were performed to correlate with the analysis. Curry *et al.* [18] employed a similar finite element formulation to study the stress distribution in laminates

with one flat face and one tapered face. They used a delamination failure criterion that is a modification of the intralamina tensile matrix mode criterion proposed by Hashin [19]. This criterion was able to correctly predict the location of failure observed in experiments, but underestimated the failure load.

Hoa *et al.* [20] investigated unidirectional laminates with two pairs of dropped plies, under axial tension loading. A three-dimensional finite element analysis was used to determine the stress and strain fields in the region of the ply drop-offs. No failure criterion was used, but a reasonable comparison was obtained with experimental values. Daoust and Hoa [21] used the same three-dimensional mesh to study various parameters affecting interlaminar stresses under static tension, bending and torsion loads. Parameters include the location of the dropped plies in the layup, the shape of the drop-off and how much it is filled with resin, the width of the laminate, and the orientation of the dropped plies. Failure is predicted using a maximum stress criterion. No experiments were performed to correlate with the analytical results.

Fish and Lee [22] investigated the delamination of tapered laminates made of 0° and ±45° plies under tension loads. A three-dimensional finite element model, including a thin interply resin layer surrounding the drop-offs, is used to calculate the out-of-plane stresses. The delamination failure criterion presented in [12], together with the average stress method, is applied to both the plies and the interply resin layers to predict the strength of the laminate. Delamination predictions based on interply resin failure showed good agreement with the experiments. This work was extended [23] to include the free-edge effect in the strength prediction of quasi-isotropic tapered laminates. The interlaminar stress state due to the free-edge effect was determined using a quasi-three-dimensional finite element model of the laminate cross-section, while the interlaminar stress state due to the ply drop-offs was calculated with a three-dimensional finite element analysis, as in [22]. The two stress states were superimposed at the root of the taper. Using the same strength prediction method, a good correlation was obtained with the experimental results. Lee and Vizzini [24] used the same tapered laminate configurations as in [22] to evaluate the interaction between the free-edge and the ply

drop-off stress concentrations. Their results indicate that the effect of the taper and the free-edge discontinuities cannot be uncoupled, and thus that only a three-dimensional model can account for this interaction. They also considered the influence of the interply resin layer thickness in the model. It was found the interlaminar shear stresses are dependent on the interply resin layer thickness, getting significantly higher as the thickness is decreased.

Several studies have also been conducted on the failure of tapered laminates using a fracture mechanics approach. Salpekar *et al.* [25] considered a laminate made of 0° and 45° plies with three ply drop-offs, under axial tensile load. A two-dimensional finite element model of the taper was used to calculate the interlaminar stresses and the strain energy release rates associated with an initial delamination at the root of the taper. Armanios and Parnas [26] conducted a study on the same tapered laminate, however using simplified energy methods to determine both the interlaminar stress state and the strain energy release rates. The results obtained with this closed-form solution are in qualitative agreement with the results reported in [25].

Murri *et al.* [27, 28] investigated the behavior of tapered laminates under tensile fatigue loads using the method proposed by O'Brien [29]. The first paper [27] considered a unidirectional 0° tapered laminate, while the second one [28] considered a multidirectional laminate similar to the one studied in [25]. The location of the initial delamination is determined from experimental observations. A two-dimensional finite element analysis is used to calculate the strain energy release rate G for this specific delamination. Then, using the curve of Gmax = f(N) of the material, the S-N curve of delamination onset for this laminate can be determined. A reasonable correlation was obtained between calculated values and experimental results.

Recently, Murri *et al.* [30] developed a fatigue life methodology for helicopter composite rotor hub flexbeams under tension and bending loads. Coupon specimens cut from a full-size glass-epoxy flexbeam were tested under these combined loads, up to failure. A two-dimensional finite element model of the tapered laminate was used to

calculate the strain energy release rates (G) associated with the experimentally observed first delamination. The number of cycles to first delamination onset was predicted by correlating these analytical G values with a curve of Gmax vs N obtained from material characterization tests. The calculated fatigue life compared well with the test results.

The research project described in [30] is very similar in its purpose to the present work. However, the methodology used for predicting the fatigue life of laminated composites structures, as well as all other fracture mechanics based methods, has a serious drawback. In order to calculate the strain energy release rates associated with a delamination and then predict the number of cycles to failure onset, one must either assume or experimentally determine the location of the initial delamination. In practical applications, such as in design of laminated composite parts, it is usually desired to evaluate the fatigue characteristics of the part without having to manufacture a specimen and perform long and costly fatigue tests. The only way the location of the first delamination can be predicted using a fracture mechanics based method is by successively calculating the strain energy release rates associated with a delamination for each location where failure could potentially initiate. This method is therefore not well suited for complex laminated composite structures such as the main rotor yoke, given the substantial computing effort that would be required.

On the other hand, failure prediction methods based on the mechanics of materials are not subject to the same limitation. A finite element model is used to determine the stress state throughout the entire laminate. Then the location where delamination will initiate under fatigue loading conditions, as well as the number of cycles to failure onset, can be predicted through the use of a suitable failure criterion. Another advantage of these methods is that they can readily be used with a commercial finite element code, without the need for custom made computational tools.

As a results of the above considerations, this work will focus on the mechanics of materials approach rather than fracture mechanics.

2 *Composite material modeling capabilities*

The finite element software package MSC/NASTRAN will be used for all finite element modeling and analysis required for the present research project. This chapter describes NASTRAN's capabilities in the modeling and analysis of laminated composite materials. Details are not provided for the standard calculations based on the classical lamination theory. Emphasis is placed on the transverse shear stiffness constitutive equations, and on the calculation of interlaminar shear stresses, which are distinctive features of NASTRAN, and are critical to the analysis.

Although use of a full three-dimensional stress analysis would have been preferable, the semi-3D analysis capabilities described in this section will be used instead, given that it is the best option available in NASTRAN.

2.1 Laminated composite materials properties

Laminated composite properties are only available with shell (plate) elements, for either four- or eight-noded quadrilateral elements (CQUAD4, CQUAD8), and for three- or six-noded triangular elements (CTRIA3, CTRIA6). The laminate is defined on a ply-by-ply basis (PCOMP entry) by inputting the thickness, the material properties (MAT8 entry) and the relative orientation of each individual lamina.

In the formulation of these laminated composite shell elements, MSC/NASTRAN uses the assumptions of classical lamination theory regarding the behavior of the laminae:

1. The laminae are perfectly bonded together.
2. The bonds are infinitesimally thin.
3. The strain varies linearly through the laminate thickness.

This approach allows the modeling of plates with coupled membrane and bending elastic behavior according to the following relations, known as the *laminate constitutive equations*:

$$\begin{Bmatrix} N \\ M \end{Bmatrix} = \begin{bmatrix} A & B \\ B & D \end{bmatrix} \begin{Bmatrix} \varepsilon^0 \\ k \end{Bmatrix} \tag{1}$$

where $\{N\} = \begin{Bmatrix} N_x \\ N_y \\ N_{xy} \end{Bmatrix}$ = stress resultants, i.e. force per unit width acting on the plate

$\{M\} = \begin{Bmatrix} M_x \\ M_y \\ M_{xy} \end{Bmatrix}$ = external moment, i.e. moment per unit width acting on the plate

$\{\varepsilon^0\} = \begin{Bmatrix} \varepsilon^0_x \\ \varepsilon^0_y \\ \varepsilon^0_{xy} \end{Bmatrix}$ = in-plane strains

$\{k\} = \begin{Bmatrix} k_x \\ k_y \\ k_{xy} \end{Bmatrix}$ = plate curvatures

$[A]$ = membrane stiffness matrix

$[D]$ = bending stiffness matrix

$[B]$ = membrane-bending coupling stiffness matrix

2.2 Calculation of transverse shear strains and stresses

Typically, a two-dimensional formulation based on the classical lamination theory does not allow the calculation of the out-of-plane stresses, or interlaminar stresses. Nevertheless, these stresses are generally present, and they play an important role in some failure mechanisms of laminated composites. A distinct feature of MSC/NATRAN plate elements is their capability to include the transverse shear stiffness:

$$\{Q\} = T_s[G]\{\gamma\} \tag{2}$$

where $\{Q\} = \begin{Bmatrix} Q_x \\ Q_y \end{Bmatrix}$ = transverse shear stress resultants

$\{\gamma\} = \begin{Bmatrix} \gamma_x \\ \gamma_y \end{Bmatrix}$ = transverse shear strains

T_s = effective transverse shear material thickness

$[G]$ = effective transverse shear stiffness matrix

MSC/NASTRAN uses an approximate procedure to evaluate both the interlaminar shear stresses and the components of the transverse shear stiffness matrix [31-32]. It is based on the assumption that the equations from elementary beam theory are applicable to plate elements, causing the effect of the twisting moments to be neglected. This is expected to yield satisfactory results in most cases.

Assuming that the x- and y- components of stress are decoupled from one another. equations from elementary beam theory can be used to calculate the interlaminar shear stresses $\tau(z)$. Demonstration will be given here for the x- direction only. For a beam of unit cross-sectional width (Figure 2), the equilibrium condition for the shaded area in the x- direction can be expressed as:

$$\int(\sigma_x + d\sigma_x)dz - \int\sigma_x dz - \tau_{xz}dx = 0 \tag{3}$$

or

$$\frac{\partial\tau_{xz}}{\partial z} = \frac{\partial\sigma_x}{\partial x} \tag{4}$$

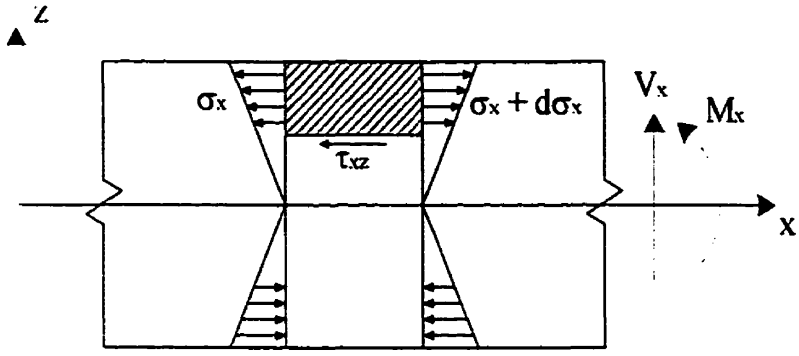

Figure 2 – Equilibrium condition, beam of unit cross-sectional width

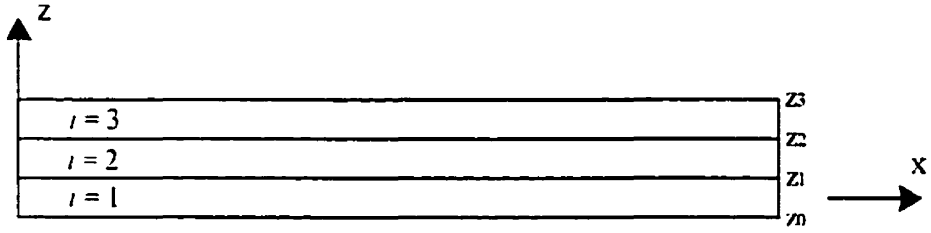

Figure 3 – Laminate configuration

Using the classical lamination theory, the strain distribution is linear through the thickness. However, the stress distribution is piecewise linear because of modulus changes between plies. Based on elementary beam theory, the axial stress distribution within the i^{th} ply (Figure 3) can be expressed as:

$$(\sigma_x)_i = -\frac{(E_x)_i(z-\bar{z}_x)}{\rho} = -\frac{(E_x)_i(z-\bar{z}_x)M_x}{(\overline{EI})_x} \qquad z_{i-1} < z < z_i \tag{5}$$

where $\bar{z}_x$ = directional bending center (location of the neutral surface)

ρ = radius of curvature of the neutral surface of the beam

$(\overline{EI})_x$ = equivalent bending stiffness of the laminate

M_x = bending moment

The location of the directional bending center $\bar{z}_x$ is given by:

$$\bar{z}_x = \frac{\sum_{i=1}^{N}(E_x)_i \frac{1}{2}\left(z_i^2 - z_{i-1}^2\right)}{\sum_{i=1}^{N}(E_x)_i (z_i - z_{i-1})} \tag{6}$$

Differentiating (5) with respect to x and substituting it into (4) yields:

$$\frac{\partial(\tau_{xz})_i}{\partial z} = \frac{\partial(\sigma_x)_i}{\partial x} = -\frac{(E_x)_i (z - \bar{z}_x) V_x}{(\overline{EI})_x} \qquad z_{i-1} < z < z_i \tag{7}$$

Then, integrating (7) with respect to z yields an expression for the interlaminar shear stress distribution within the i^{th} ply:

$$(\tau_{xz})_i = -\frac{(E_x)_i V_x}{(\overline{EI})_x}\left(\frac{z^2}{2} - \bar{z}_x z\right) + C_i \qquad z_{i-1} < z < z_i \tag{8}$$

The known boundary conditions at the ply interfaces are used to determine the constants C_i. For the first ply at the bottom surface ($i = 1$ and $z = z_0$), $\tau_{xz} = 0$ and therefore:

$$C_1 = -\frac{V_x (E_x)_1}{(\overline{EI})_x}\left(-\frac{z_0^2}{2} + \bar{z}_x z_0\right) \tag{9}$$

Then at the interface between the first and the second plies ($z = z_1$):

$$(\tau_{xz})_1 = -\frac{V_x (E_x)_1}{(\overline{EI})_x}\left[\frac{1}{2}\left(z_1^2 - z_0^2\right) - \bar{z}_x (z_1 - z_0)\right] \tag{10}$$

and

$$(\tau_{xz})_2 = -\frac{V_x (E_x)_2}{(\overline{EI})_x}\left[\frac{z_1^2}{2} - \bar{z}_x z_1\right] + C_2 \tag{11}$$

The value of C_2 is obtained by equating (10) and (11):

$$\begin{aligned} C_2 &= (\tau_{xz})_1 + \frac{V_x (E_x)_2}{(\overline{EI})_x}\left(\frac{z_1^2}{2} - \bar{z}_x z_1\right) \\ &= -\frac{V_x}{(\overline{EI})_x}\left[\left\{\frac{1}{2}\left(z_1^2 - z_0^2\right) - \bar{z}_x (z_1 - z_0)\right\}(E_x)_1 - \left\{\frac{z_1^2}{2} - \bar{z}_x z_1\right\}(E_x)_2\right] \end{aligned} \tag{12}$$

Therefore, at the interface between the second and the third plies ($z = z_2$), we obtain:

$$\begin{aligned} (\tau_{xz})_2 = -\frac{V_x (E_x)_1}{(\overline{EI})_x}&\left[\frac{1}{2}\left(z_1^2 - z_0^2\right) - \bar{z}_x (z_1 - z_0)\right] \\ &- \frac{V_x (E_x)_2}{(\overline{EI})_x}\left[\frac{1}{2}\left(z_2^2 - z_1^2\right) - \bar{z}_x (z_2 - z_1)\right] \end{aligned} \tag{13}$$

In general, for a given ply i such that $z_{i-1} < z < z_i$, the transverse shear is given by:

$$(\tau_{xz})_i = (\tau_{xz})_{i-1} - \frac{V_x (E_x)_i}{(\overline{EI})_x}\left[\frac{1}{2}\left(z^2 - z_{i-1}^2\right) - \bar{z}_x (z - z_{i-1})\right] \tag{14}$$

And at any ply interface z_i, the shear is therefore:

$$(\tau_{xz})_i = \frac{V_x}{(\overline{EI})_x}\sum_{j=1}^{i} (E_x)_j T_j \left[\bar{z}_x - \frac{1}{2}\left(z_j + z_{j-1}\right)\right] \tag{15}$$

where

$$T_j = z_j - z_{j-1}$$

This can now be used to evaluate the components of the transverse shear stiffness matrix [G]. We define an equivalent transverse shear modulus $\overline{G}$ for the laminate, based on the expression for the transverse shear strain energy U:

$$U = \frac{1}{2}\int \frac{(\tau(z))^2}{G(z)}dz = \frac{1}{2}\frac{V^2}{\overline{G}T} \tag{16}$$

where T = laminate thickness

Only the evaluation of an uncoupled x- component of the equivalent transverse shear moduli will be demonstrated here. Equation (16) can thus be rewritten in the following form:

$$\frac{1}{\overline{G}_x} = \frac{T}{V_x^2}\int_{-T/2}^{T/2} \frac{(\tau_{xz}(z))^2}{(G_x)}dz = \frac{T}{V_x^2}\sum_{i=1}^{N}\int_{z_{i-1}}^{z_i} \frac{(\tau_{xz}(z))_i^2}{(G_x)_i}dz \tag{17}$$

Equation (14) could be substituted into (17) and integrated. A better form of (14) for this purpose is:

$$(\tau_{xz})_i = \frac{V_x(E_x)_i}{(\overline{EI})_x}\left[(f_x)_i - \frac{1}{2}\left(z^2 - z_{i-1}^2\right) + \bar{z}_x\left(z - z_{i-1}\right)\right] \tag{18}$$

where

$$(f_x)_i = -\frac{1}{(E_x)_i}\sum_{j=1}^{i-1}(E_x)_j\left[\frac{1}{2}\left(z_j^2 + z_{j-1}^2\right) - \bar{z}_x\left(z_j - z_{j-1}\right)\right] \tag{19}$$

Now, substituting (18) into (4), and then integrating with respect to z yields:

$$\frac{1}{\overline{G}_x} = \frac{T}{(\overline{EI})_x^2} \sum_{i=1}^{N} \frac{1}{(G_x)_i} (R_x)_i \tag{20}$$

where

$$(R_x)_i = (E_x)_i^2 T_i \left[\left\{ (f_x)_i + (\bar{z}_x - z_{i-1}) T_i - \frac{1}{3} T_i^2 \right\} (f_x)_i \right.$$
$$+ \left\{ \frac{1}{3} (\bar{z}_x - 2z_{i-1}) - \frac{1}{4} T_i \right\} \bar{z}_x T_i^2 \tag{21}$$
$$\left. + \left\{ \frac{1}{3} z_{i-1}^2 + \frac{1}{4} z_{i-1} T_i + \frac{1}{20} T_i^2 \right\} T_i^2 \right]$$

$$T_i = (z_i - z_{i-1})$$

This equation allows to calculate the uncoupled x- component of the equivalent transverse shear modulus $\overline{G}_x$, or $\overline{G}_{11}$. Note that the moduli for individual plies $(G_x)_i$ are provided through user input. Equation (20) can be generalized in the following form to provide for calculation of the other components:

$$\frac{1}{[\overline{G}_{k\ell}]} = \frac{T}{(\overline{EI})_{kk}^2} \sum_{i=1}^{N} \frac{1}{(G_{k\ell})_i} (R_k)_i \qquad k, \ell = 1, 2 \tag{22}$$

where

$$(\overline{EI})_{11} = D_{11} \cdot \frac{12}{T_3} \tag{23}$$

$$(\overline{EI})_{22} = D_{22} \cdot \frac{12}{T_3}$$

Finally, because in general $\overline{G}_{12} \neq \overline{G}_{21}$, an average of the two values will be used for the coupling terms. The transverse shear stiffness matrix is therefore as follows:

$$[G] = \begin{bmatrix} \overline{G}_{11} & (\overline{G}_{12})_{avg} \\ (\overline{G}_{12})_{avg} & \overline{G}_{22} \end{bmatrix} \tag{24}$$

3 *Main rotor yoke finite element model*

3.1 General description

The main rotor yoke is a '+' shaped single piece structure made of glass fiber laminated composite. The yoke is the primary load bearing part within the main rotor hub assembly. The tapered section of each 'arm', called the flexure, allows for elastic deformation of the rotor hub in order to accommodate the blades flapping motion. The thick central section, and the thick outboard end of each arm, are used for attachment with the main rotor hub and with the blades, respectively (Figure 1).

The yoke is made of three different forms of the same E-glass / epoxy material: roving, unidirectional tape and woven fabric. Continuous 0° roving belts (four belts across each pair of opposing arms) are manufactured separately, and then laid up in a mold with numerous ± 45° fabric and 0° tape plies of various length to achieve the tapered flexure profile. The layup is therefore not constant across the laminate.

The main rotor yoke is subjected to a complexe dynamic loading environment: axial centrifugal force CF, cyclic beamwise bending loads F_b (due to the blades vertical flapping motion) and cyclic chordwise bending loads F_c (due to the blades lead-lag motion). These loads are shown schematically on Figure 4.

Finally, note that specific locations (sections) along one of the yoke arms are referred to in terms of 'station', i.e. the distance in inches between the section and the rotor axis.

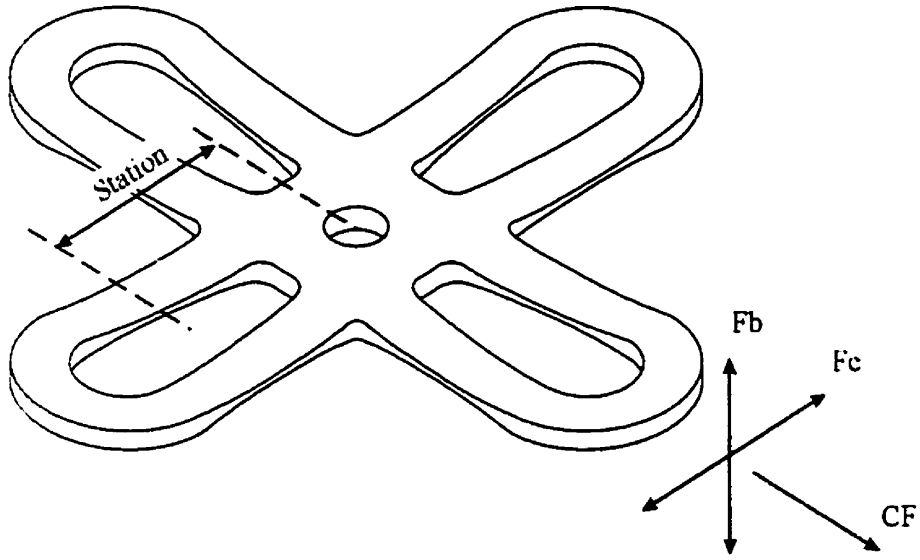

Figure 4 – Main rotor yoke loading environment

3.2 Model overview

A global model of the Main Rotor Yoke was created using NASTRAN laminated composite shell elements capabilities. Detailed modeling of the yoke's laminated composite structure was carried out, in order for the model to correctly reproduce the global response of the part, but also to yield detailed local ply stress and strain results (within the limitations due to the use of two-dimensional elements).

The yoke geometry used for developing of the finite element model was obtained from the CATIA CAD model of the part. Using the midplane of this solid model, a tridimensional shell model was created, and served as a geometrical basis to develop the NASTRAN finite element model (Figure 5). Because of the existing symmetries in the geometry and internal structure of the yoke, only one of the four yoke arms was modeled. In reality, if one considers the exact laminating sequence, there is a slight difference in the layup of the two pairs of opposing arms due to the position of the roving belts, but in order to keep the model reasonably simple, the four arms were considered as identical. When required, a more complete model of the yoke can be easily obtained by copying this one-arm model.

Four-noded quadrilateral isoparametric shell elements (CQUAD4) were used, together with several three-noded triangular isoparametric shell elements (CTRIA3), when required by the geometry. Although NASTRAN also has higher order shell elements that can be used for composite materials applications, these elements were not used at first in order to limit the size of the model. It will be shown in section 3.5.4 that for the present model, the use of higher-order elements would not result in any significant improvement in precision.

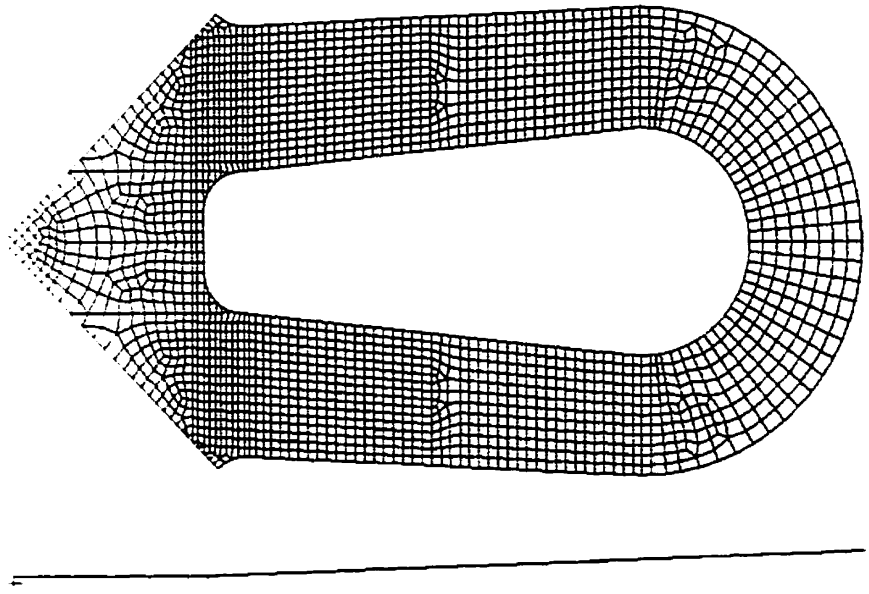

Figure 5 – Yoke finite element shell mesh

3.3 Materials and layup

3.3.1 Ply material properties

The main rotor yoke laminate structure is made of three different composite ply materials: glass fiber/epoxy roving, glass fiber/epoxy tape, and glass fiber/epoxy woven fabric. Roving and tape plies are unidirectional (Figure 6), while fibers in the plain

weave fabric are at 0°/90° (Figure 7). The x, y and z axes are in the longitudinal, transverse and normal directions, respectively.

Within the scope of the present study, the raw prepregs materials are not available for testing. It is therefore not possible to perform any experiment to characterize the material parameters (moduli and strengths). However, most of the required material characterization has already been performed. Those material parameter values that cannot be found in the available documentation are approximated based on material symmetries, and on similar data for the other materials. Table 1 summarizes the material properties used in this study. E_{xx}, E_{yy}, E_{xy}, E_{xz}, E_{yz} are the longitudinal, transverse, in-plane shear, out-of-plane shear (x-z plane) and out-of-plane shear (y-z plane) modulus, respectively. ν_{xy} is the Poisson's ratio, and ρ is the density. X_t, Y_t, X_c, Y_c, S_{xy} and S_b are the longitudinal tensile, transverse tensile, longitudinal compressive, transverse compressive, in-plane shear and interlaminar shear strengths, respectively.

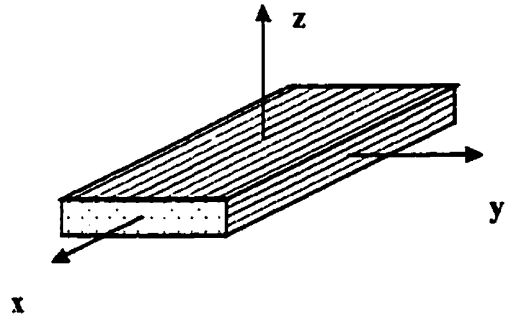

Figure 6 – Structure of tape and roving unidirectional plies

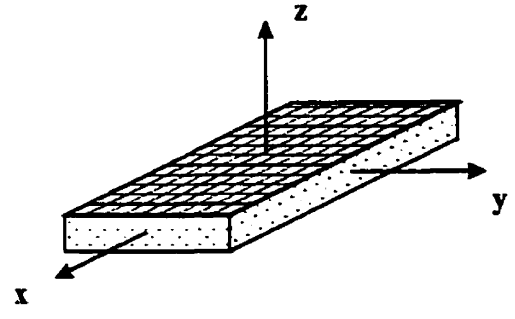

Figure 7 – Structure of woven fabric plies

		Roving	Tape	Fabric
Exx	Msi (Gpa)	Data removed for protection of proprietary information		
Eyy	Msi (Gpa)			
Exy	Msi (Gpa)			
Exz	Msi (Gpa)			
Eyz	Msi (Gpa)			
ν_{xy}	--			
ρ	lb/in^3 (kg/m^3)			
Xt	ksi (Mpa)			
Yt	ksi (Mpa)			
Xc	ksi (Mpa)			
Yc	ksi (Mpa)			
Sxy	ksi (Mpa)			
Sb	ksi (Mpa)			

Table 1 – Material parameters of the yoke glass fiber/epoxy materials

For a given ply direction, the NASTRAN orthotropic material definition does not allow input of different values for tension and compression moduli. However, the available data shows that all three ply materials are significantly stiffer in compression than in tension. Because of the loads the yoke is subjected to, it will deform mainly in bending, meaning that roughly half of the laminate is under tension while the other half is under compression. It is therefore assumed that by using an average value of the tensile and the compressive moduli, the global stiffness of the model will approach that of the real part. This will be verified using experimental yoke stiffness data (section 3.5).

The bonding shear stress limit, which represents the interlaminar strength of the laminate, must have the same value for all three ply materials. This is because the interlaminar strength depends mainly on the resin properties. Indeed, available values of interlaminar shear strength for these materials are found to be very similar. The lowest of the three values (i.e. interlaminar shear strength of fabric) is used in the model.

3.3.2 Composite laminates

As described in Section 3.1, the tapered geometry of the yoke is obtained by gradually dropping internal plies along the flexure. The only way such a tapered laminate can be modeled with NASTRAN is using a succession of flat laminates decreasing in thickness. The continuous taper is therefore approximated by a series of discrete steps, as shown in Figure 8. For the yoke model (one arm), a total of 60 different sub-laminates are required in order to obtain a geometry reasonably close to that of the part (Figure 9). The finite element mesh was created so that it coincides with this partition of the model.

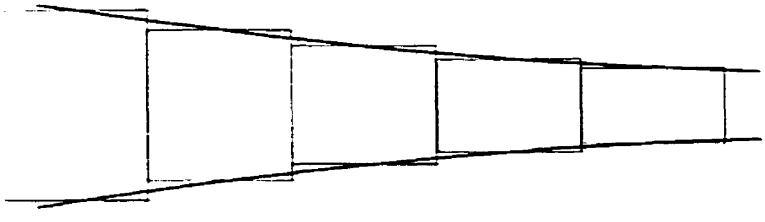

Figure 8 – Approximating the taper with a succession of flat laminates

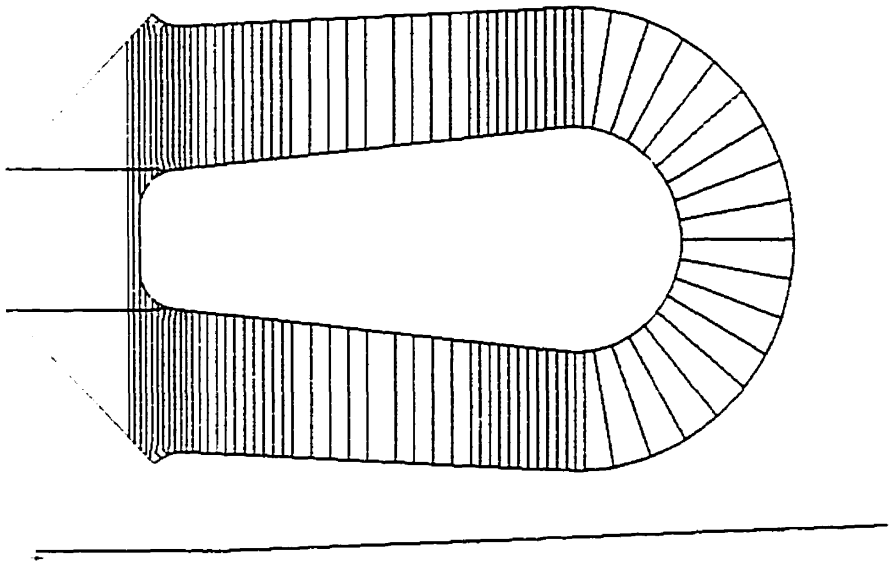

Figure 9 – Yoke model partition into sub-laminates

3.3.3 Individual ply thickness

The cured ply thickness is data that is readily available, but it is only a mean value for given curing conditions. If a higher pressure is applied during the cure cycle, more resin will flow out of the laminate, resulting in thinner plies. Moreover, for a complex laminated part cured in a closed mold, as for the main rotor yoke, the pressure applied to the composite plies may not be constant in all areas. This would cause the cured ply thickness to vary from one area to another. It is therefore required to determine realistic cured ply thickness values for the model. The nominal cured ply thickness for the tape and fabric materials are given in Table 2. The nominal thickness of the roving layers is given by the dimension of the tool [33] used to manufacture the belts by filament winding. Using these values and the exact yoke laminating sequence, the global thickness of the laminate is calculated at various locations along the flexure, and then compared to the actual yoke mold shape. Figure 10 shows that if the nominal ply thickness values are used, the resulting model is significantly too thick.

Several combinations of reduced roving, tape and fabric ply thickness values have been studied, in order to bring the thickness of the model closer to the yoke mold shape. Given that the roving belts run on the entire length of the yoke arm, varying their thickness causes the model thickness to vary of an equal amount on the entire length of the flexure. On the other hand, the fabric and tape layers are used to build up the tapered geometry of the yoke. Therefore, varying the fabric and/or tape ply thickness will cause the model thickness to vary much more in the inboard and outboard ends than in the thinner part of the flexure. The reduced ply thickness values given in Table 2 are found to yield a global model thickness that is very close to the yoke mold geometry, as shown in Figure 11. This combination is therefore retained for the yoke shell model. Note that any of the ply thickness combinations studied overestimated the thickness of the inboard area, while underestimating the thickness of the outboard area.

Ply thickness		**Roving**	**Fabric**	**Tape**
Nominal value	in.	0.054	0.0092	0.0092
	(mm)	(1.37)	(0.234)	(0.234)
Reduced value	in.	0.050	0.0080	0.0080
	(mm)	(1.27)	(0.020)	(0.020)

Table 2 – Cured ply thickness, nominal and reduced values

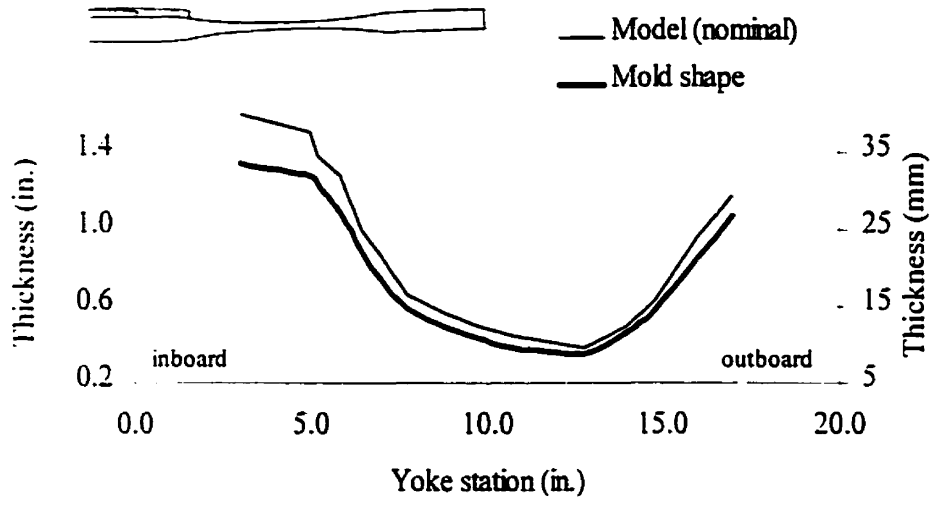

Figure 10 – Model thickness with nominal values of ply thickness

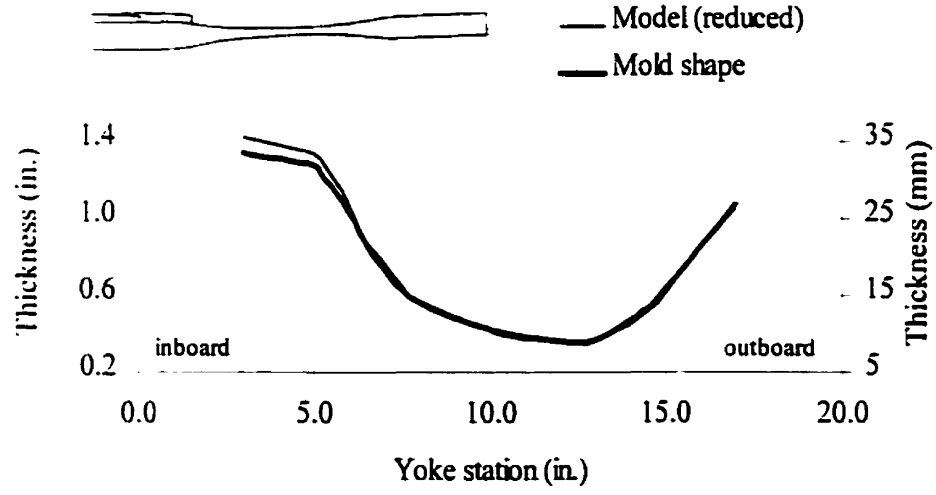

Figure 11 – Model thickness with reduced values of ply thickness

3.3.4 Postprocessing considerations

As described in section 3.3.2, the tapered yoke flexure is modeled by a succession of flat laminates decreasing in thickness. In the NASTRAN model definition, the layups for each of these laminates are defined independently from each other. The code does not allow the user to keep track of a given ply across different laminates, or to identify which plies have been dropped between two adjacent laminates. For example in Figure 12, a five plies laminate reduces to three plies after internal plies are dropped. In Figure 12(a), the bottommost ply is identified as ply 5 in laminate A, while the same ply is identified as ply 3 in laminate B. Clearly in this case, it is not possible to postprocess the analysis results by "global layer", i.e. with respect to the actual composite plies from which the part is built. The individual plies identification would need to be consistent between the various laminates, as in Figure 12(b).

A technique was developed to overcome this problem, and allow for appropriate and meaningful postprocessing of the results. It requires to modify the layup of the laminates defined in the model. When one or more plies are dropped between a given laminate and the adjacent one, instead of completely removing the dropped plies from the layup, these plies are kept in the laminate as extremely thin dummy layers, about 12 orders of magnitude thinner than the real plies. This method is based on the assumption that if the thickness ratio between the real plies and the thin dummy plies is large enough, the presence of the "dummy" plies will not have any noticeable influence on the results. The validity of this assumption was verified using a simple representative test case, as described in appendix A.

However, the technique previously described presents a major drawback, in that it significantly increases the size of the model, and the time required for computations. The main area of interest for the present study is the inboard region, from the thick central part up to the thinnest part of the flexure, at station 13.0 (Figure 14). In order to limit the size of the model, only the laminates in that portion of the yoke were modified by the "dummy plies" technique.

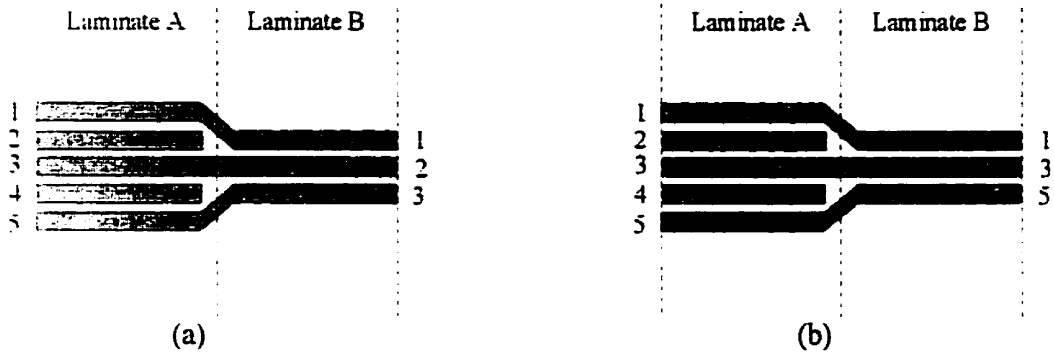

Figure 12 – Individual plies in a laminate (a) as defined in NASTRAN, (b) required for meaningful results postprocessing

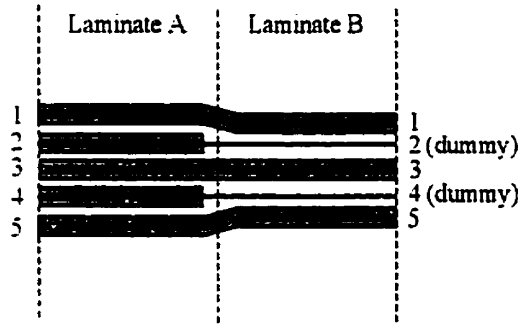

Figure 13 – New laminate definition using thin dummy layers

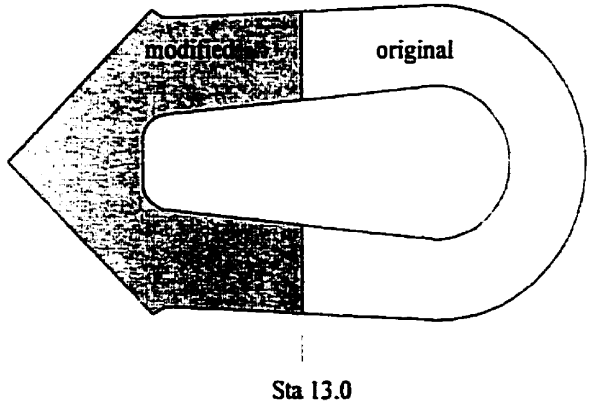

Figure 14 – Laminates modified to allow for ply-by-ply results postprocessing

3.4 External loads

In actual use, external loads are applied to each arm of the yoke through a CF elastomeric bearing which is attached to the yoke by an aluminium adaptor (Figure 15). The elastomeric bearing is free to twist, so that the yoke does not react torsion. Therefore, the yoke is only subjected to centrifugal force, and to chordwise and beamwise bending loads. It can be assumed that the resultant of these external loads is applied on the adaptor at the CF elastomeric bearing focal point, which is at station 19.0 on the centerline of the arm (see Figure 16).

The actual load distribution along the yoke/adaptor contact interface is unknown. In the model, the load distribution along this interface will directly depend on how the adaptor and the yoke/adaptor interface are modeled. The adaptor is assumed to be a rigid body. It is also assumed that there is no friction between the yoke and the adaptor, and thus that only normal contact forces are transmitted at this interface. Pairs of coincident nodes are created all along the yoke/adaptor interface. The adaptor is represented by a single rigid element (an RBE2 element) connecting a node of each pair to the central node where external loads are applied (Figure 16). The radial contact at the yoke/adaptor interface is modeled using contact (CGAP) elements between the coincident interface nodes. The out-of-plane contact between the flanges on the adaptor and the top/bottom surfaces of the yoke is modeled by constraining the coincident nodes to move together in the vertical plane. Thus, the true area of contact between the adaptor and the yoke is modeled, making the load application more realistic.

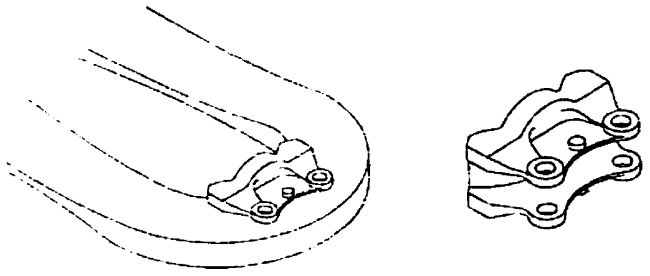

Figure 15 – Yoke outboard adaptor

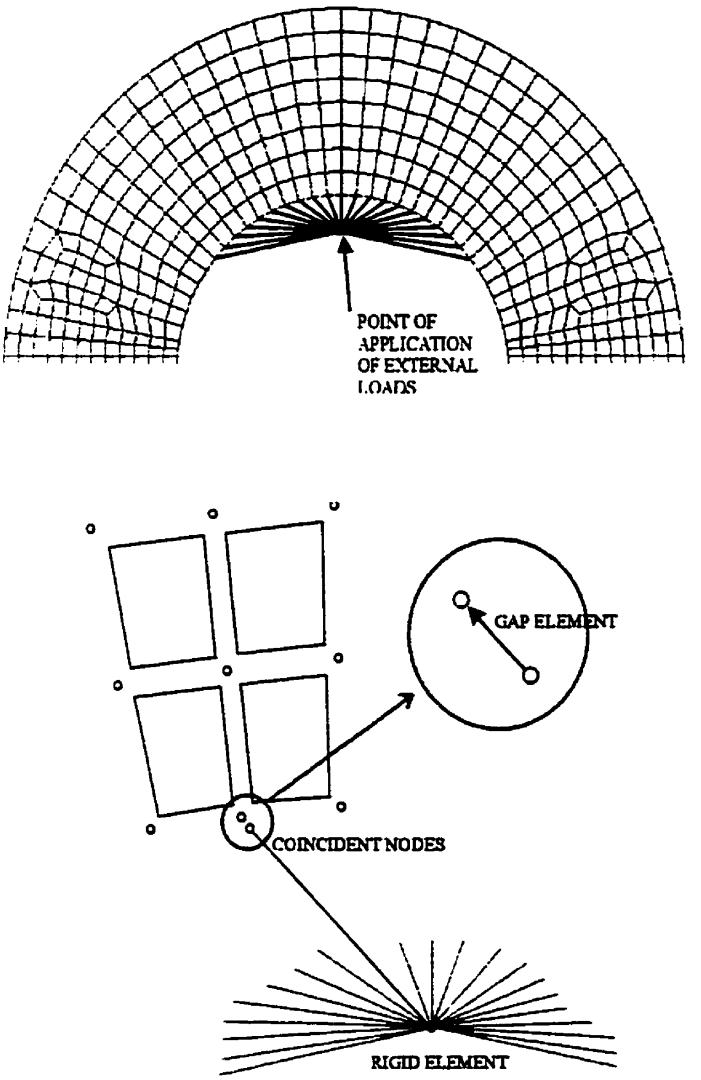

Figure 16 – Modeling of the yoke-adaptor radial interface

3.5 Verification of model stiffness

3.5.1 Experimental data

As a preliminary validation for the yoke finite element model developed in this study, the stiffness of the model is compared with experimental data. The stiffness, or load – deflection experimental data was gathered during strain gages calibration tests performed at the Structural Test Laboratory of Bell Helicopter Textron, Fort Worth [34]. Those experiments were performed on a rigid test fixture. All the supporting parts in the the main rotor hub assembly (Figure 1) were included in the test assembly, in order to reproduce the environment encountered by the yoke in actual flight conditions. The bending loads – beamwise or chordwise – were applied to one arm at the time, while the central section of the yoke was rigidly maintained on the test fixture. The outboard adaptors were not installed, thus the external loads were applied directly on the outboard yoke surface (Figure 17).

3.5.2 Modeling and analysis

In order for the model to properly represent the experimental configuration, the stiffness of the two arms adjacent to the one being loaded needs to be taken into account. A finite element model corresponding to three-quarters of the yoke (Figure 18) is therefore obtained by simply copying the one-arm model previously described. The external loads are applied to the model directly on the appropriate shell element node.

All six degrees of freedom are constrained on boundary A (Figure 18), which represents the location of the assembling bolts that rigidly maintain the yoke on the test fixture. On the two boundaries B and C, all degrees of freedom are constrained except T_x (in local coordinates) to allow for radial expansion. Even though the latter restraints are slightly over-constraining the model, they are located far enough from the area of interest on the loaded arm to assume that they have a negligible influence on the results.

For both chordwise and beamwise loading conditions, calculations are performed both using a linear solution sequence (SOL 101) and using a non-linear

solution sequence (SOL 106). This will allow to evaluate whether it is required to perform non-linear (iterative) calculations, which are significantly more time consuming than the one-step linear calculations.

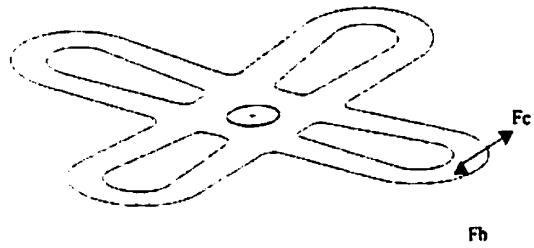

Figure 17 – External loads for calibration experiments

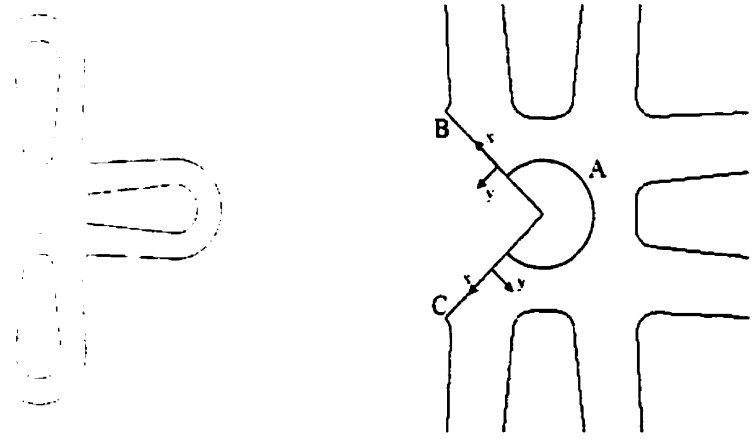

Figure 18 – Three-arm model and restraints

3.5.3 Analysis results

The analytical load-deflection results obtained for beamwise and chordwise bending are shown in Table 3 (Figure 19) and Table 4 (Figure 20), respectively. Under beamwise bending loads, the non-linear analysis yields results that are slightly more precise than those obtained with a linear analysis. This is because the structure experiences large deflections. The global stiffness matrix needs to be reevaluated based on an updated model geometry, and this requires the use of an iterative non-linear

solution sequence. The beamwise bending stiffness of the finite element model, as obtained with the non-linear analysis, is shown to be about 9% lower than the stiffness of the actual part, which is considered to be an acceptable correlation.

Under chordwise bending loads, the linear and non-linear solutions yield virtually the same load-deflection results. The yoke being much stiffer chordwise than beamwise, no relatively large displacements are involved and therefore a non-linear analysis is not required. However, the load-deflection results obtained are obviously wrong, the model being too stiff by as much as 55%. According to NASTRAN analysis specialists, such results are completely unexpected. They could be due to the element formulation yielding to shear stiffness problems, when used for modeling tapered laminates. However, the cause of the problem is very difficult to assess here because of the complexity of the model (geometry, materials and laminate layup). In order to confirm the source of the problem, much additional work would be required. One would need to perform a series of experiments on various simple test specimens, and correlate the results with the correponding finite element analyses. This work was not conducted within the scope of this study; the raw prepreg materials are not available, therefore it is not possible to manufacture the required test specimens.

Load (lbs)	Beamwise deflection (inches)				
	Experimental	Linear	%error	Non-linear	%error
97	0.293	0.355	21.2 %	0.356	21.6 %
194	0.636	0.710	11.6 %	0.710	11.6 %
292	0.977	1.069	9.4 %	1.063	8.8 %
389	1.294	1.424	10.0 %	1.407	8.8 %
486	1.61	1.779	10.5 %	1.745	8.4 %

Load (N)	Beamwise deflection (mm)				
	Experimental	Linear	%error	Non-linear	%error
431.5	7.44	9.02	21.2 %	9.04	21.6 %
863.0	16.15	18.03	11.6 %	18.03	11.6 %
1298.9	24.82	27.15	9.4 %	27.00	8.8 %
1730.3	32.87	36.17	10.0 %	35.74	8.8 %
2161.8	40.89	45.19	10.5 %	44.32	8.4 %

Table 3 – Experimental and analytical beamwise bending load-deflection results

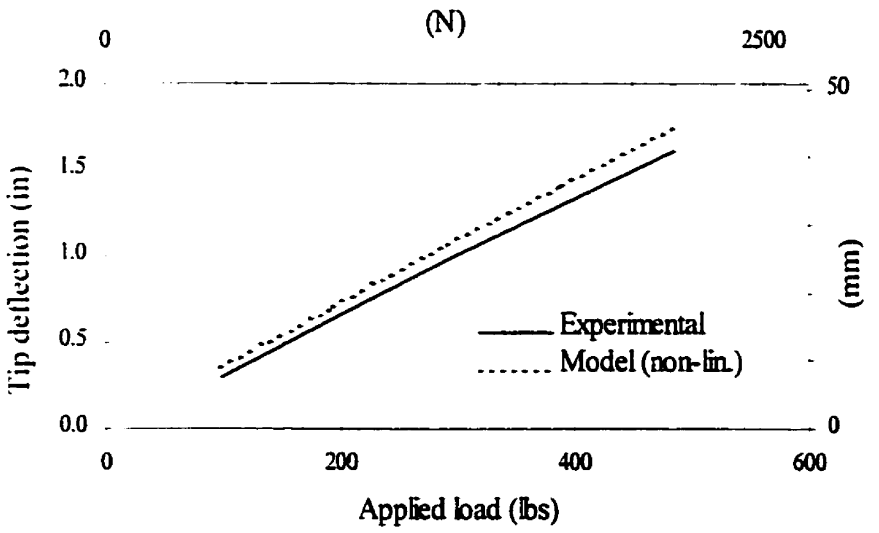

Figure 19 – Experimental and analytical beamwise bending load-deflection

Load (lbs)	Chordwise deflection (inches)				
	Experimental	Linear	%error	Non-linear	%error
467	0.028	0.0138	-50.8 %	0.0138	-50.8 %
934	0.059	0.0275	-53.3 %	0.0275	-53.3 %
1402	0.092	0.0413	-55.0 %	0.0413	-55.0 %
1869	0.126	0.0551	-56.3 %	0.0551	-56.3 %
2336	0.160	0.0689	-56.9 %	0.0689	-56.9 %

Load (N)	Chordwise deflection (mm)				
	Experimental	Linear	%error	Non-linear	%error
2077.3	0.711	0.351	-50.8 %	0.351	-50.8 %
4154.6	1.499	0.699	-53.3 %	0.699	-53.3 %
6236.4	2.337	1.049	-55.0 %	1.049	-55.0 %
8313.7	3.200	1.400	-56.3 %	1.400	-56.3 %
10391.0	4.064	1.750	-56.9 %	1.750	-56.9 %

Table 4 – Experimental and analytical chordwise bending load-deflection results

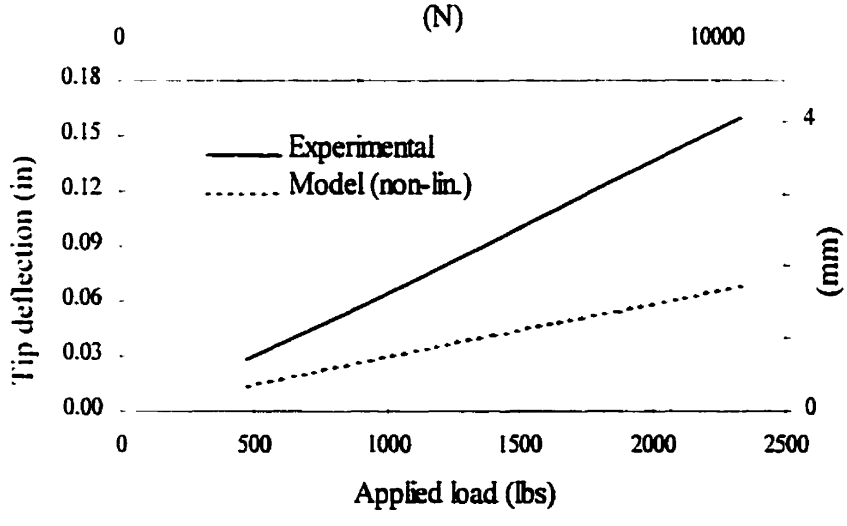

Figure 20 – Experimental and analytical chordwise bending load-deflection

3.5.4 Higher order shell elements

It is desired to verifiy if the element topology used in the model is appropriate or if higher order shell elements, also available in NASTRAN, would yield more accurate results. A second three-arm model is therefore created using higher order (quadratic) elements: eight-noded quadrilateral shells (CQUAD8) and six-noded triangular shells (CTRIA6). The composite layup, boundary conditions and loads are exactly the same as in the model described in the previous section. A load-deflection analysis is performed with this second model. A non-linear solution is used for beamwise bending while a linear solution is used for chordwise bending. Results are given in Table 5 and Table 6, respectively.

Load	**Beamwise deflection** (inches)				
(lbs)	**Experimental**	**Linear**	**%error**	**Quadratic**	**%error**
97	0.293	0.356	21.6 %	0.355	21.2 %
194	0.636	0.710	11.6 %	0.711	11.8 %
292	0.977	1.063	8.8 %	1.070	9.5 %
389	1.294	1.407	8.8 %	1.425	10.1 %
486	1.610	1.745	8.4 %	1.780	10.7 %

Load	**Beamwise deflection** (mm)				
(N)	**Experimental**	**Linear**	**%error**	**Quadratic**	**%error**
431.5	7.44	9.04	21.6 %	9.02	21.2 %
863.0	16.15	18.03	11.6 %	18.06	11.8 %
1298.9	24.82	27.00	8.8 %	27.18	9.5 %
1730.3	32.87	35.74	8.8 %	36.20	10.1 %
2161.8	40.89	44.32	8.4 %	45.21	10.7 %

Table 5 – Beamwise bending load-deflection results as a function of element topology (non-linear solution sequence)

Load (lbs)	Chordwise deflection (inches)				
	Experimental	Linear	%error	Quadratic	%error
467	0.028	0.0138	-50.8 %	0.0138	-50.7 %
934	0.059	0.0275	-53.3 %	0.0276	-53.2 %
1402	0.092	0.0413	-55.0 %	0.0415	-54.9 %
1869	0.126	0.0551	-56.3 %	0.0553	-56.1 %
2336	0.160	0.0689	-56.9 %	0.0691	-56.8 %

Load (N)	Chordwise deflection (mm)				
	Experimental	Linear	%error	Quadratic	%error
2077.3	0.711	0.351	-50.8 %	0.351	-50.7 %
4154.6	1.499	0.699	-53.3 %	0.701	-53.2 %
6236.4	2.337	1.049	-55.0 %	1.054	-54.9 %
8313.7	3.200	1.400	-56.3 %	1.405	-56.1 %
10391.0	4.064	1.750	-56.9 %	1.755	-56.8 %

Table 6 – Chordwise bending load-deflection results as a function element topology (linear solution sequence)

The beamwise stiffness obtained with the original model (linear element topology) is shown to correspond better to the experimental results than the stiffness calculated using the higher-order elements. In chordwise bending, the calculated stiffness is the same using either element topology. Moreover, the use of higher order shell elements results in a significant increase in computation time, due to an increased number of degrees of freedom in the model. Therefore, there are no advantages in using higher order elements in the present model.

3.6 Verification of calculated stress field

3.6.1 Experimental data

An extensive fatigue test program [35] was conducted on the main rotor yoke. These fatigue tests were performed on an hydraulic test bench specially designed for this purpose, which can subject the entire yoke to realistic multidirectional loads: a static tensile load (corresponding to the centrifugal load) as well as oscillatory beamwise and chordwise bending loads (Figure 21). Note that while the axial tensile load (CF) and the beamwise bending load (Fb) are the same on each arm, the chordwise bending loads are applied in opposite directions on adjacent arms. All the supporting parts in the main rotor hub assembly (Figure 1) were included in the test assembly, in order to reproduce the environment encountered by the yoke in actual flight conditions. The yokes used in this fatigue test program are basically the same as those used in the experimental portion of the current research program, except that they were made with a different resin system.

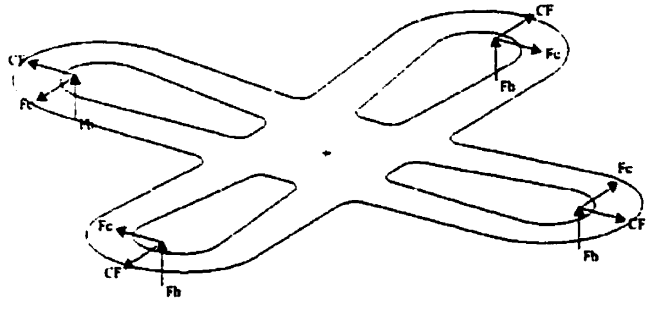

Figure 21 –External loads applied to the yoke in fatigue tests

This test program provided typical load vs number of cycles to failure (S-N) data for each specimen tested. The results available also include information on the nature of the failures and the approximate location where these failures were observed. Although these fatigue test results cannot be used to perform a quantitative validation of the model (because of the difference in the resin system), part of these results can be used in a qualitative evaluation of the model. The objective is to verify whether the areas where failures were observed in the fatigue experiments correspond to areas in the model where high stress levels are encountered.

3.6.2 Determination of external loads

The bending loads to which the yoke is subjected to are usually described in terms of resultant bending moments at a specific location, usually station 7.0 or station 8.75. Experimentally, the resultant bending moments are directly measured using properly calibrated strain gages. In the present finite element model, the loading of the yoke is only known in terms of the external forces applied to the outboard adaptor, as described in section 3.4. Consequently, in order to correlate the finite element model with the existing data, a relationship must be established between the external forces applied to the model and the resultant bending moments.

The resultant chordwise bending moment at a given location of the flexure can be directly calculated based on the unloaded configuration. The moment arm of Fc is assumed not to vary upon loading, given that chordwise deflections remain very small. The load Fc being applied at station 19.0 (see section 3.4), the resultant chordwise bending moment at station X will be given by:

$$M_{c,X} = F_c \cdot (19.0 - X) \tag{25}$$

A different approach is required to calculate the beamwise bending moment, because the structure undergoes large flapping deformations. Both Fb and the centrifugal load contribute to the resulting beamwise bending moment. While the moment arm of Fb could be assumed constant, the moment arm of the centrifugal force is strongly dependent on the deformed geometry, as shown in Figure 22. The directions of the forces, Fb and CF, are assumed to remain constant, even under large deflections. The relationship between the load Fb applied to the yoke and the resultant beamwise bending moment can therefore not be defined in terms of an explicit equation. For a given loading condition, a non-linear finite element analysis must first be performed to obtain the final deformed shape of the yoke under the combined Fb and CF loads. The deflection results obtained are then used to determine the new moment arms (λ_x and λ_z) of the external forces. The resultant beamwise bending moment is given by:

$$M_{b\_X} = F_b \cdot \lambda_x - CF \cdot \lambda_z \tag{26}$$

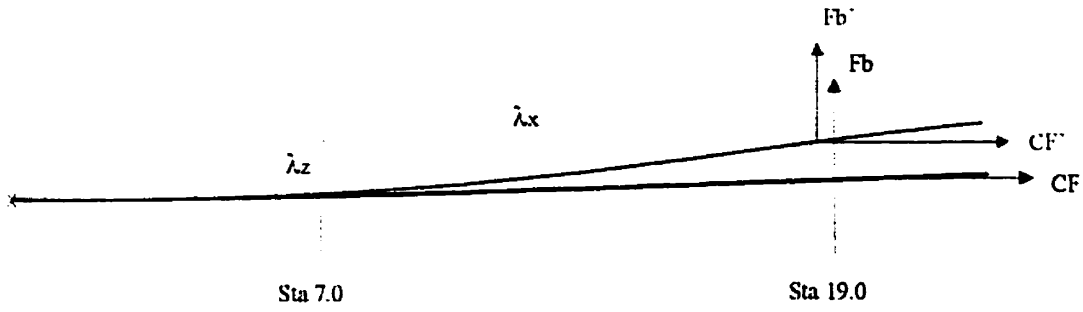

Figure 22 – Applied loads vs deformed and undeformed geometry

Using this procedure systematically, one can develop curves of resultant beamwise bending moment as a function of the applied Fb load, for a given value of centrifugal force, CF. Figure 23 shows an example of such a curve for a constant centrifugal force of 33150 lbs.

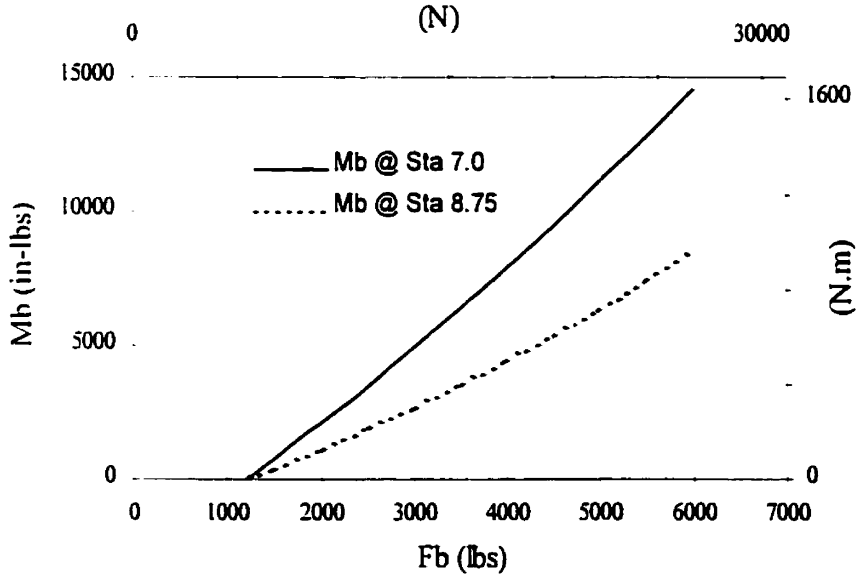

Figure 23 – Curves of resultant beamwise bending moment (Mb) as a function of the beamwise bending load (Fb) applied, for 33150 lbs of centrifugal load.

3.6.3 Analysis and results

Because of the symmetries that exist in the external loads applied to the yoke (Figure 21), only one yoke arm with proper boundary conditions is required in the model in order to properly represent the test conditions. All six degrees of freedom are constrained on boundary A (Figure 24), which represents the location of the assembling bolts that rigidly maintain the yoke and the supporting parts. The nodes on the two boundaries B and C are constrained in Ty, Rx and Rz (in local coordinates) because of the existing symmetries both in the geometry of the part and in the loads applied.

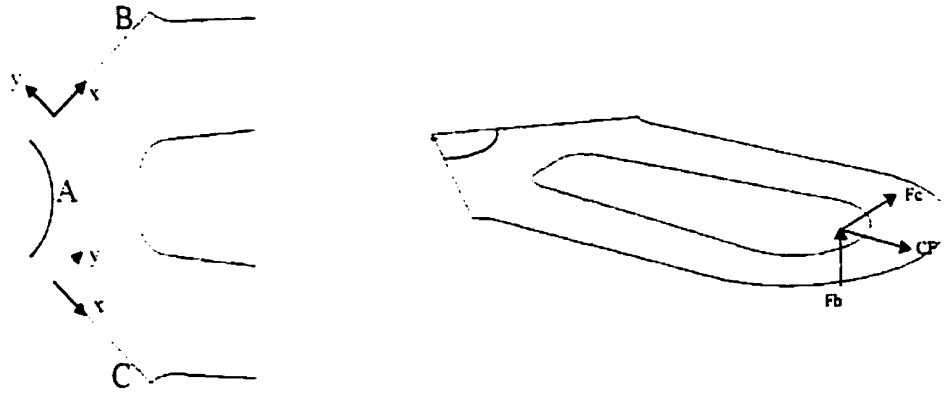

Figure 24 – Inboard restraints on the model for yoke fatigue tests

A qualitative comparison is to be performed between static stress analysis results and the fatigue experimental results. In order for that comparison to be valid, only the oscillatory part of all stress components must be considered. This is achieved by performing two separate finite element analyses for each test condition. One analysis uses the maximum peak loads (steady loads plus oscillatory loads), while the other analysis uses the minimum peak loads (steady loads minus oscillatory loads). After the analyses are completed, the two stress results sets are subtracted.

All of the failures observed during yoke fatigue experiments were due to delamination [35]. Based on examination of the fracture faces, these delaminations were determined to have occurred due to interlaminar shear. Most of them were located in the

same area of the yoke, between station 6.0 and station 9.0, on the bottom side of the flexure between the lower roving belt and the outermost group of unidirectional tape plies (Figure 25). Detailed information on the exact location of the delaminations (i.e. at which specific ply interface they were observed) is not available.

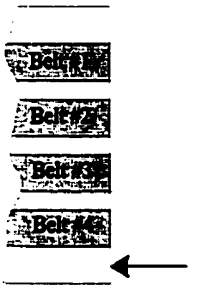

Figure 25 – Approximate location of delaminations in fatigue experiments

An example of the oscillatory stresses distribution calculated with the model is shown in Figure 26 through Figure 29, here for fatigue experiment #1. Note that very similar results are obtained for the other test specimens. All results are shown for the same fabric ply (ID 107), which is located between the lower roving belt and the outermost group of unidirectional tape plies, i.e. where delaminations were observed experimentally. These results indicate that the laminate failures observed during fatigue experiments coincide well with with highly stressed areas, more specifically with high values of the interlaminar shear stress and normal tensile (σ_z) stress.

This qualitative correlation suggests that the yoke finite element model is reasonably representative of the yoke, and is able to properly simulate its properties. A more detailed validation of the yoke model will be carried out in Chapter 4.

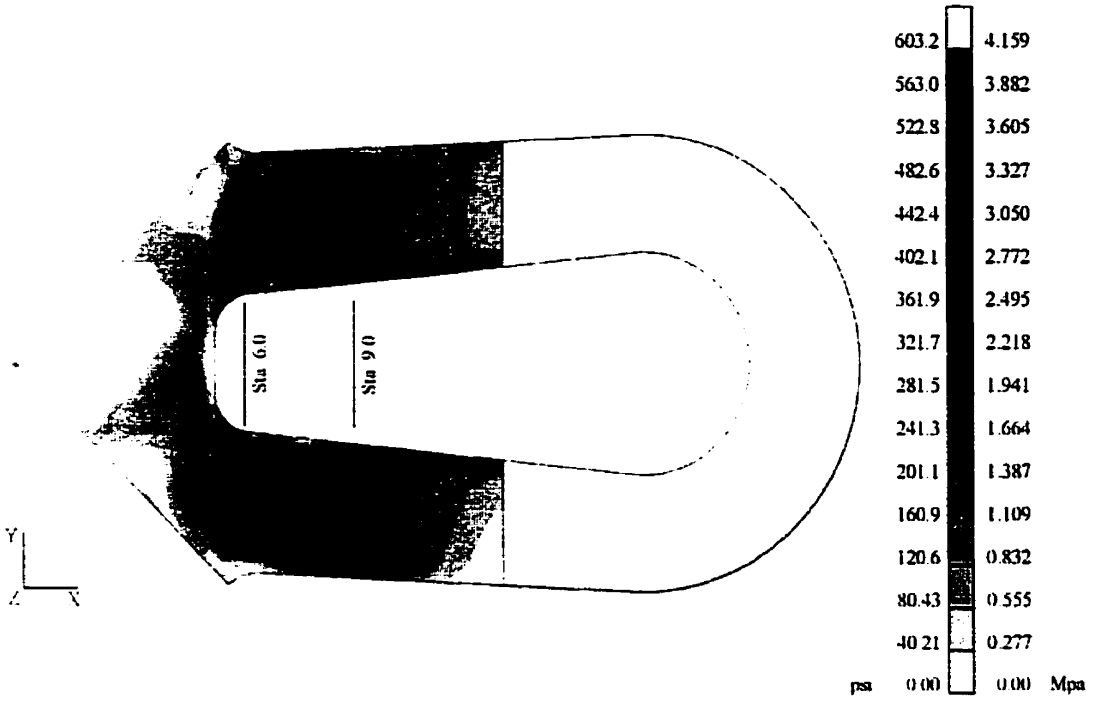

Figure 26 – Yoke fatigue test #1 : interlaminar shear oscillatory stress results (layer 107)

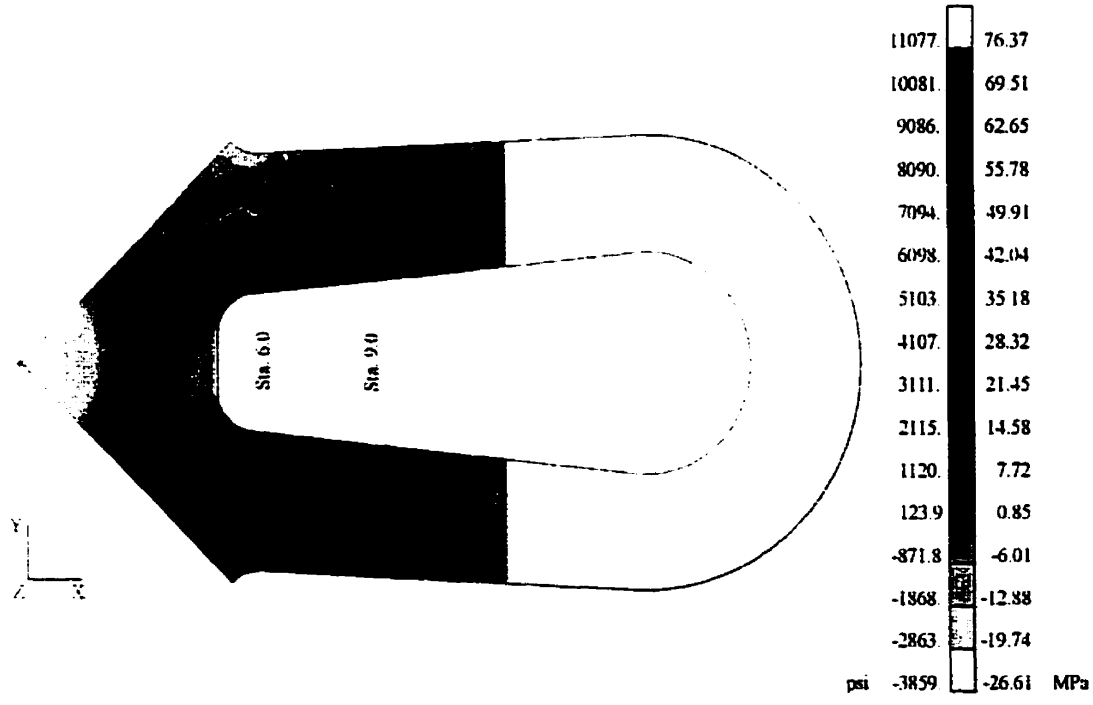

Figure 27 – Yoke fatigue test #1 : σ_x oscillatory stress results (layer 107)

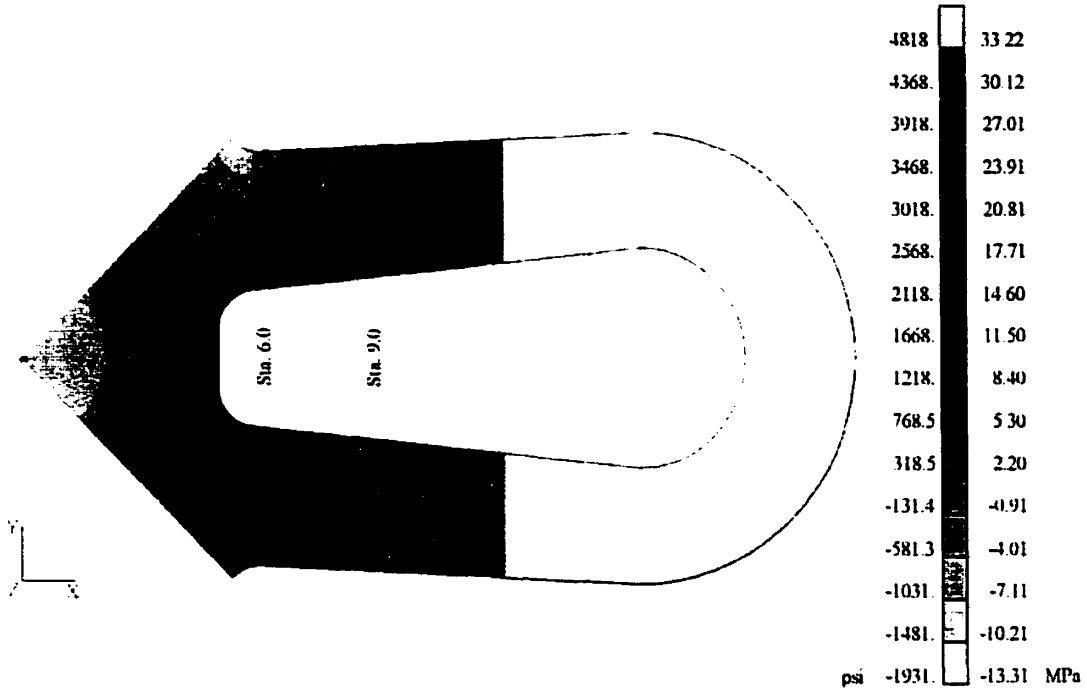

Figure 28 – Yoke fatigue test #1 : σ_y oscillatory stress results (layer 107)

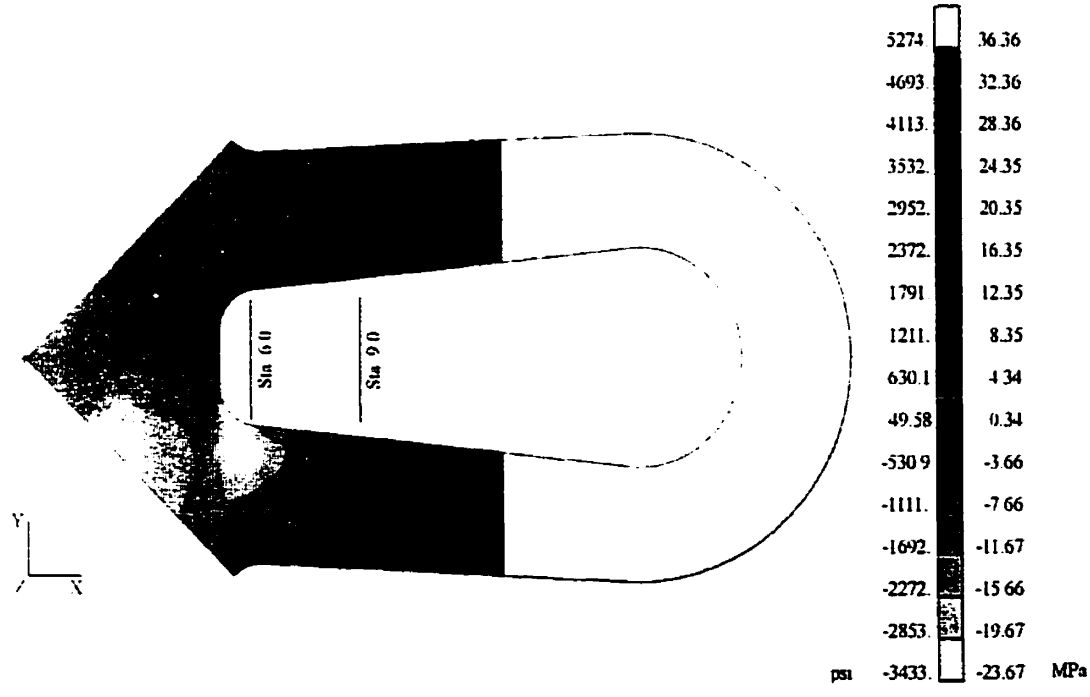

Figure 29 – Yoke fatigue test #1 : σ_{xy} oscillatory stress results (layer 107)

4 *Yoke specimen static experiments and analysis*

A series of experiments is to be performed on specimens cut out of actual main rotor yokes. The purpose of these experiments is to generate data on the static and fatigue properties of the yoke as a whole, under simple and controlled testing conditions. The experimental results are to be correlated with analytical results from a finite element analysis of the specimen, in order to develop a model for predicting the fatigue behavior of the yoke.

4.1 Introduction

In actual flight conditions, the yoke is subjected to a complex combination of steady and oscillatory loads: oscillatory beamwise bending loads, oscillatory chordwise bending loads, and a steady centrifugal load (Figure 4). In order to experimentally recreate such a loading environment, a complex test apparatus would be required. In the present study, it is desired instead to subject the yoke specimens to much more simple test conditions.

The major deformations experienced by the yoke in flight are due to the blades' flapping motion, i.e. beamwise deflection of the yoke flexure. In a previous study [35], even though complex multiaxial loads were applied to the yoke during the experiments, the measured beamwise bending moment was considered to be the determinant parameter in delamination of the yoke. The present study will therefore concentrate on this specific component of the yoke loading environment. Only beamwise bending loads are to be applied to the yoke specimen in the experiments.

4.2 Specimen geometry

Several points need to be considered when selecting the proper specimen geometry to be used in the experiments, to make sure that the results obtained from specimen testing are as representative as possible of the entire yoke mechanical behavior.

Most of the failures observed in previous yoke fatigue experiments [35] were delaminations originating at the edges of a flexure. This suggests that the edge effect plays an important role in these failures. If a narrow beam-like specimen was to be cut in the yoke flexure, the width-to-thickness ratio of this specimen would be significantly smaller that in the actual yoke, thus increasing the influence of the edge effect on the failure. It is therefore desirable that the selected test specimen geometry includes the full width of the yoke flexure, to ensure that they will be representative of the yoke mechanical properties. Also, examining these results from previous fatigue experiments, it is observed that most of the delaminations occurred between station 6.0 and station 9.0 on the flexure. This can therefore be considered a critical area for failure. In order to allow for meaningful correlation between the yoke specimen and the entire yoke, it is desired that this portion of the flexure be included in the test specimen. Care must be taken when selecting the geometry of the specimen and designing the test fixture, so that the test fixture does not induce any local stress concentrations in that critical area. The yoke test specimen must also include a portion of the thick and flat inboard section of the yoke, in order to provide a good attachment area to install the specimen on the testing machine.

Two specimen shapes can be obtained, which meet all of the above requirements (see Figure 30). Specimen type #1 can provide up to eight specimens per yoke. However, the portion of the specimen that can be used for installation on the testing machine is relatively small, and not well aligned with the flexure. Specimen type #2 appears to have better overall characteristics: the portion of the specimen that can be used for installation on the testing machine is much wider, and allows to properly constrain the specimen beamwise. Although only four specimens of this type can be obtained from a yoke, this specimen shape is selected for the present study due to its superior geometrical characteristics (Figure 31). The flexure will be cut at station 13.0, just after it reaches its minimum thickness.

It should be noted that the two yokes made available for testing are actual production parts that were rejected because of local defects in the composite laminated

structure (porosity, inclusions or fibers misalignment). Great care was taken, when selecting the specific arms to be used as specimens, to ensure that all of these known defects are avoided.

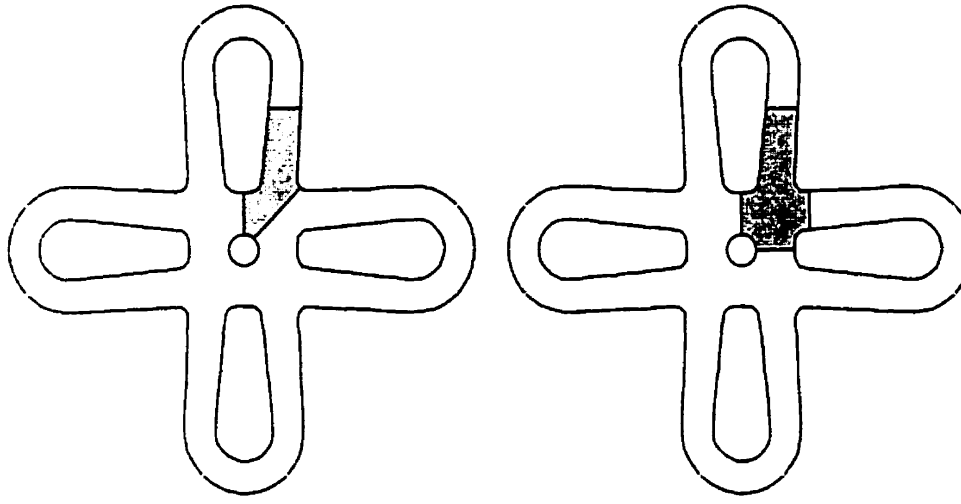

Figure 30 – Two types of yoke test specimens

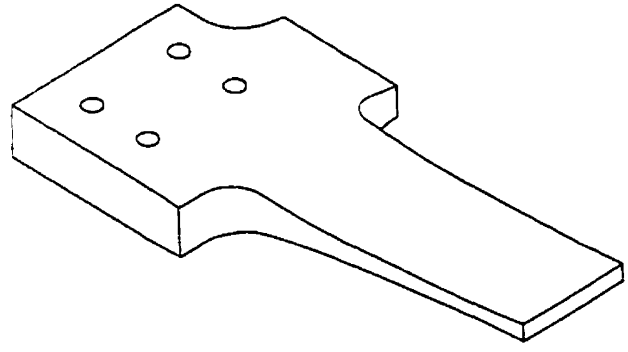

Figure 31 – Selected test specimen geometry

4.3 Test apparatus

All experiments were conducted in the Composite Materials Laboratory, in the Department of Mechanical Engineering of McGill University. The yoke specimens were tested on an MTS 810 hydraulic load frame, having a capacity of 25 metric tons.

A specially designed test fixture (Figure 32) is used to install the specimens on the testing machine. The upper cantilevered part of the test fixture is attached to the steady crossbar of the load frame. The test specimen is then fastened to this part by means of four bolts. Beamwise bending loads are applied to the test specimen at station 12.0. via a horizontal steel cylinder fixed on the moving hydraulic head of the load frame. The cylinder extends across the entire width of the flexure.

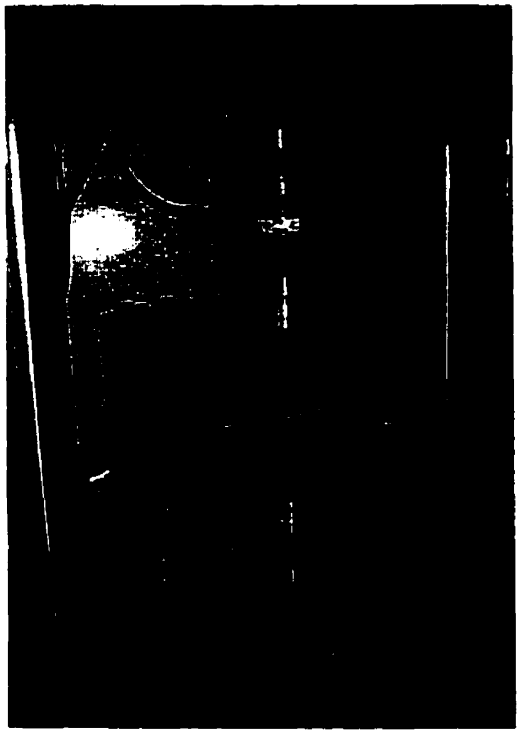

Figure 32 – Test apparatus

4.4 Finite element model of the test specimen

A finite element model of the yoke test specimen (Figure 33) was developed based on the global yoke model described in Chapter 3. The geometry and laminated composite structure of the specimen are exactly the same as in the corresponding area of the global yoke model. The finite element mesh is also very similar, except for the thick end of the specimen which was completely remeshed in order to allow for proper modeling of the specimen's boundary conditions.

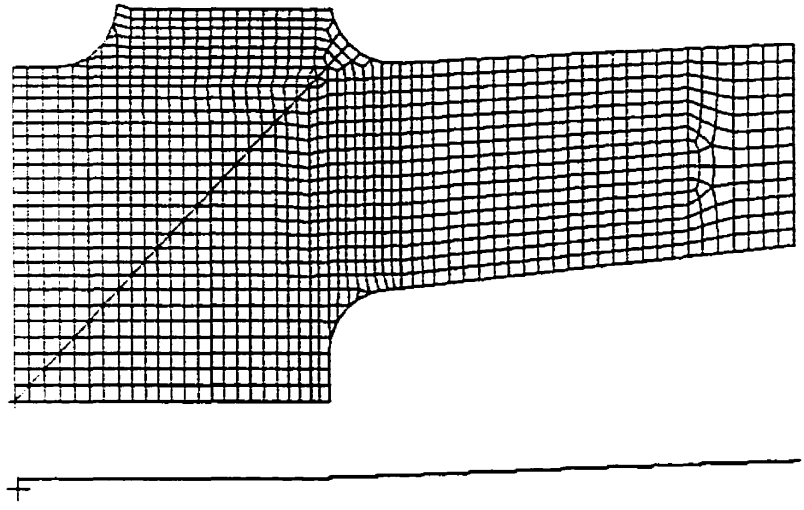

Figure 33 – Finite element model of the test specimen

As described in section 4.3, the thick end of the test specimen is rigidly attached to the test fixture by means of four bolts. This is represented in the model by constraining the nodes corresponding to the location of the four bolts, so that no displacement is allowed in all six degrees of freedom.

It is also necessary to properly model the displacement restraint imposed to the specimen where it contacts with the test fixture. The area where the yoke and the test fixture are in contact is determined by the tapered geometry of the yoke, rather than by the geometry of the fixture, as shown in Figure 34. The surface of contact is therefore as

indicated by the shaded area in Figure 35. The test fixture is modeled by adding a set of fully constrained nodes to the model. These new nodes are coincident with the shell element nodes located on the sides of the surface of contact. Contact (CGAP) elements are defined between these coincident nodes, in order to simulate the contact between the two surfaces (Figure 35).

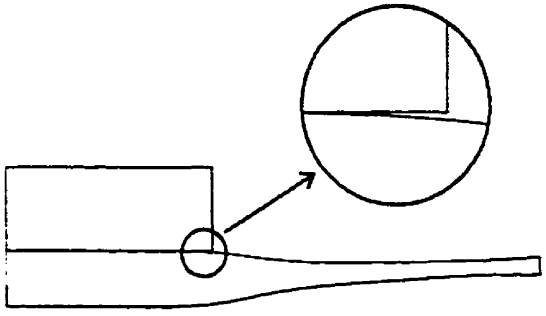

Figure 34 – Surface of contact between the yoke specimen and the test fixture

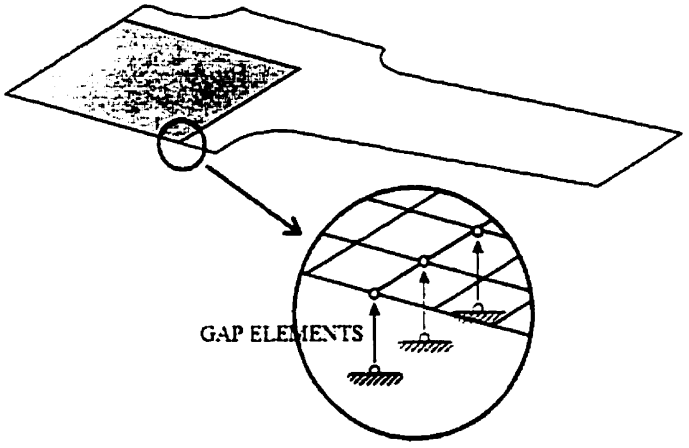

Figure 35 – Restraints on the specimen model due to the test fixture

The external bending load is applied to the test specimen by means of a cylinder pushing on the outboard end of the flexure. In order to simulate properly the loading configuration, the cylindrical loading head needs to be included in the finite element analysis. It is modeled by a rigid element (Figure 36), and constrained so that it

can only move vertically without any rigid body rotation. The contact between the loading head and the test specimen is modeled using contact (CGAP) elements, defined between the nodes of the cylinder and the corresponding nodes on the specimen model. The result is that upon loading, all the shell element nodes at the interface undergo the same vertical displacement.

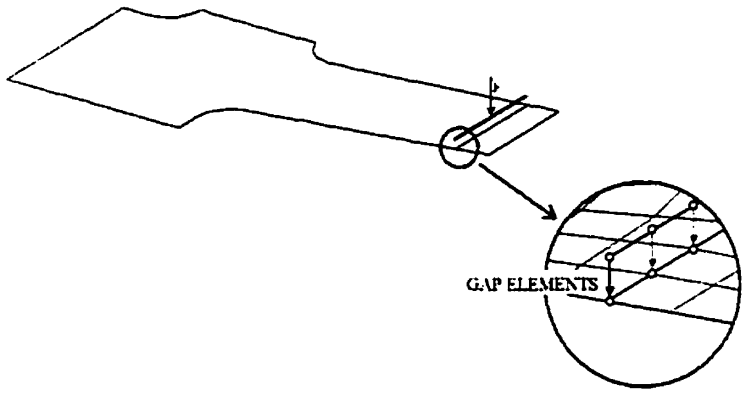

Figure 36 – Specimen model loading

4.5 Verification of boundary conditions

In order to assess the validity of the proposed boundary and loading conditions, an arbitrary load is applied to the model, and the distribution of forces at the inboard and outboard interfaces of the model is qualitatively evaluated. Note that in order for the gap elements to behave as non-linear elements (i.e. different stiffness values in tension and in compression), the analysis must be run using a non-linear solution sequence.

The contact forces between the specimen and the test fixture are as shown in Figure 37. On the edge between points A and C, the distribution of contact forces is asymmetrical, because the external load applied by the cylinder is eccentric with respect to the bolted attachment. The edge between points B and C is free of contact forces; this can be explained by the edge A-C acting as a pivot line. The distribution of contact forces observed in the model therefore appears to be in good agreement with the loading

configuration. It can be noted in the results that the model exhibits a load concentration at point B. It is however very unlikely that a similar concentrated reaction exists in the actual experimental conditions, because the contact between the specimen and the fixture at this point is a smooth curve, rather than a sharp edge (Figure 34). This characteristic of the geometry cannot be taken into account in the model; therefore, the resultant local rise in stresses will simply be ignored in the results.

Figure 38 shows the load distribution at the interface between the loading head and the surface of the specimen. The calculated load distribution is clearly asymmetric: much more pressure is applied on one side of the flexure than on the other side. This phenomenon was confirmed experimentally during fatigue tests (Chapter 5), by an apparent wear of the surface of the specimen under the loading head. The surface wear is observed to be much more severe at the location where higher contact forces are predicted by the model. It is believed that because the external loads applied through the cylinder are eccentric with respect to the specimen's inboard constraints, the flexure tends to warp under bending, causing the observed asymmetrical load distribution.

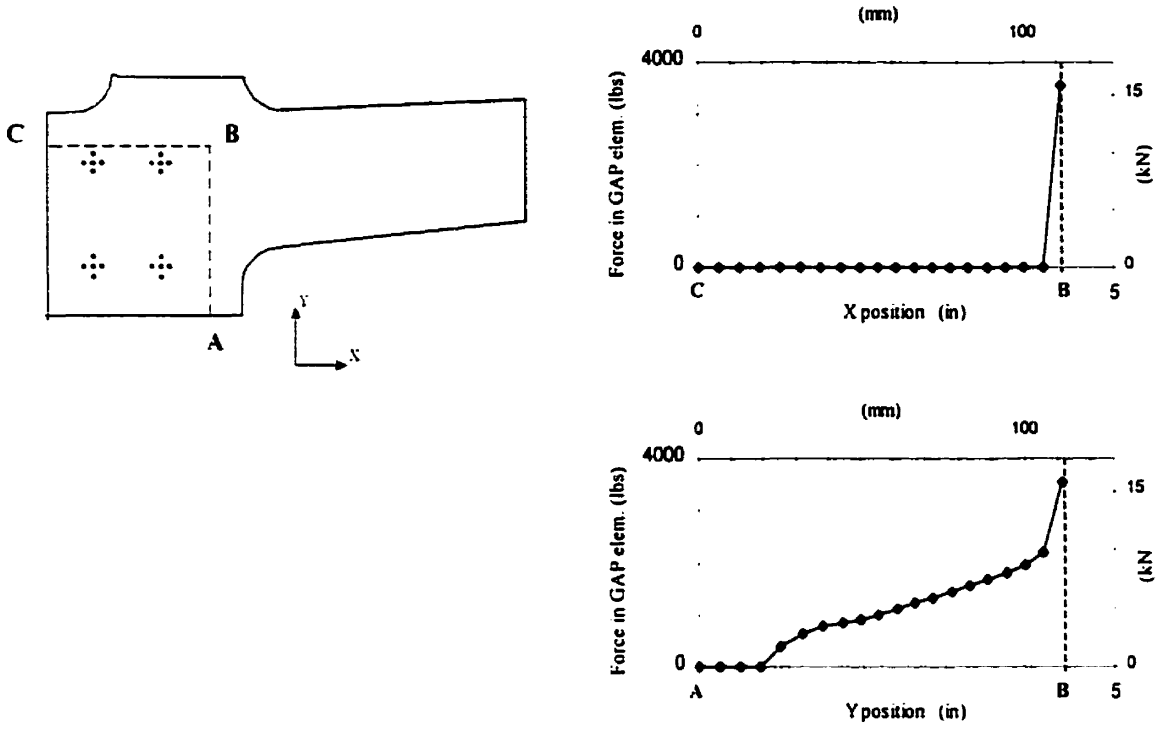

Figure 37 – Contact forces at the interface between the specimen and the test fixture

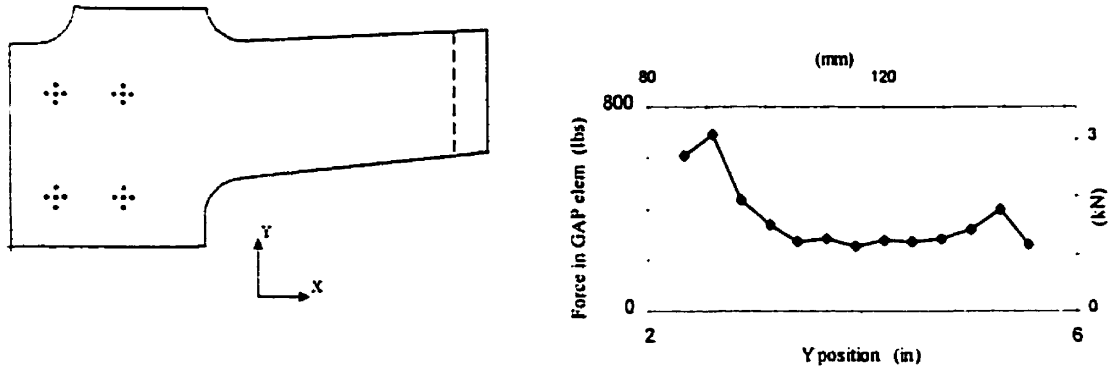

Figure 38 – Contact forces at the interface between the loading head and the specimen

4.6 Verification of the model stiffness

In Chapter 3, the stiffness of the global yoke model was verified against experimental load-deflection data from tests performed on a complete yoke arm. In this study, similar quasi-static non-destructive experiments are performed on the yoke specimens, and results are then correlated with the stiffness calculated with the specimen finite element model. Given that the test specimen finite element model is basically a portion of the global yoke model, these new experimental load-deflection results will provide an additional validation of the stiffness of the global yoke model.

Displacement is gradually applied to the end of the specimen under test, and load-displacement data points are recorded at regular intervals by the testing machine controller. The displacement values are given by the relative position of the loading head. Corresponding analytical results are calculated with the specimen model. Comparison between the experimental and analytical load-deflection curves (Figure 39) suggests that the model has a slightly higher stiffness than what is observed experimentally. However, a closer look at the experimental setup revealed that a movement occurs in the test assembly when load is applied to the specimen. The exact source of this unwanted deflection in the fixture could not be determined, whether it is the test fixture that deflects, or part of the testing machine, or both. This will affect the measure of displacements, but not the loads applied to the specimen. Given that all specimen testing will be done under load control, this situation will therefore not pose a problem in further results.

In order to obtain a valid measurement of the specimen stiffness, an additional measurement of the displacement must be taken directly on the test specimen. An extensometer is therefore fitted on the lower surface of the specimen, with the two branches 1" apart at stations 7.0 and 8.0, giving a measurement of the mean surface strain over that area (Figure 40). The surface of the specimen was sanded locally prior to installation of the extensometer, in order to increase the surface roughness, and thus avoid slippage of the extensometer when the specimen deflects.

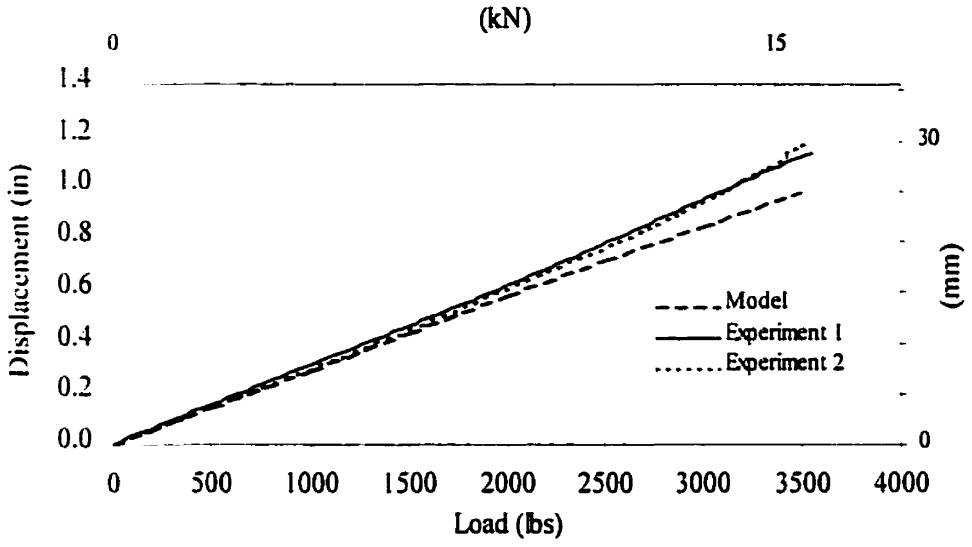

Figure 39 – Test specimen, analytical and experimental load – deflection curves

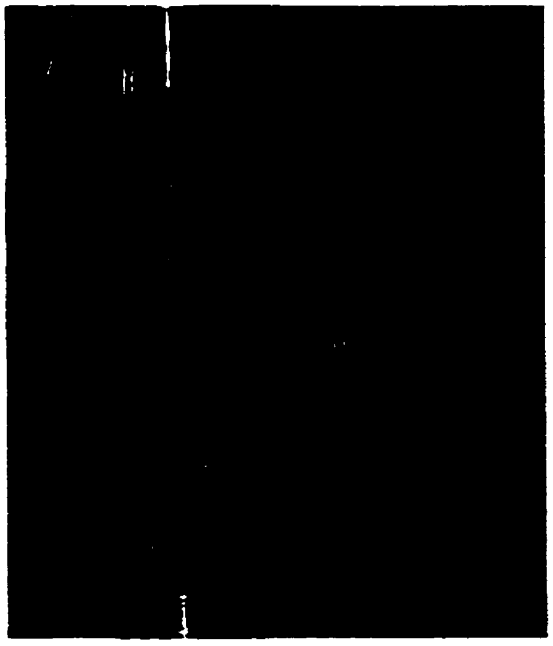

Figure 40 – Extensometer installation

The experimental load-strain curves obtained for two test specimens are shown in Figure 42 along with the equivalent analytical curve calculated with the finite element model. The analytical mean surface strains, corresponding to the experimental values measured with the use of the extensometer, are calculated based on the assumption that the beamwise bending neutral plane is located at the midplane of the specimen flexure. The relative displacements (translations and rotations) of two nodes located in the center of the flexure at station 7.0 and station 8.0 are used to calculate the required surface strains, as shown in Figure 41.

Comparison between the experimental and analytical load-strain curves shows that the stiffness of the model is lower than what is observed experimentally. This is consistent with what was found in Chapter 3 for the full yoke model. However, the error on the calculated stiffness is greater, here about 20%. This is still considered a reasonable correlation. The increased error on the calculated stiffness is probably due to the method used to derive the mean surface strains. The experimentally measured surface strains are believed to be accurate, since very similar results were obtained with two different test specimens. However, the surface strains calculated based on the finite element model are not exact values, because of the assumption made on the location of the bending neutral axis. The bending neutral axis is likely not to be exactly at the midplane, given that the laminate is not flat (2° preset angle upwards) and the layup is not symmetric in the upper half and lower half of the flexure.

Note that in Figure 39, the model seems to underpredict displacement results, while in Figure 42 the model overpredicts strain results. In fact, this is due to the error discussed on page 53: part of the displacement measured experimentally occurs in the test fixture rather than within the specimen.

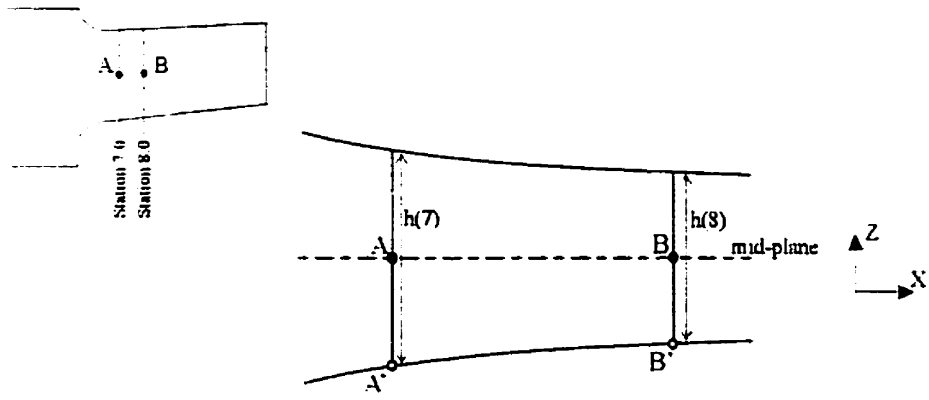

Figure 41 – Calculation of mean surface strains

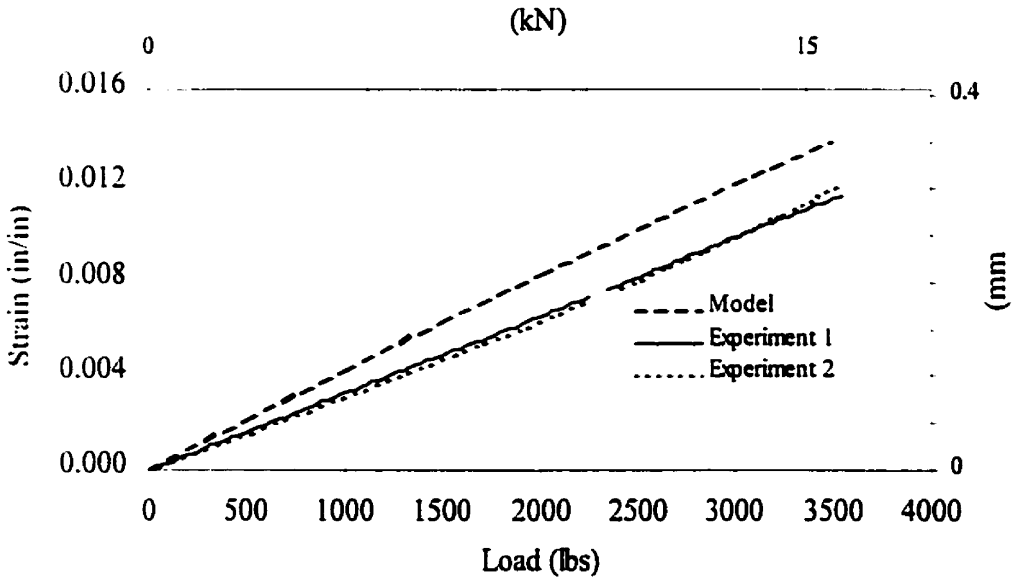

Figure 42 – Test specimen, analytical and experimental load – strain curves

4.7 Prediction of static failure

The model needs to properly simulate the properties of the test specimen under a static load, including the ability to predict the ultimate load that the specimen can carry. Without meeting this requirement, the model could not be further used to predict the fatigue behavior of the part. This comes down to verify the validity of the stress results calculated with the model. Although the present model is not capable of calculating detailed three-dimensional stress fields, it should, however, be able to reasonably predict the areas of high stresses, therefore allowing estimating the location of failure and ultimate failure load.

Quasi-static destructive experiments were performed on two test specimens to determine the ultimate static load the specimen can withstand. The tests were performed under displacement control; the loading head displacement was monotonically increased at the rate of 0.1 mm/sec until the first failure was observed. In both cases, the test specimen showed no sign of damage prior to catastrophic delamination failure.

For the first specimen tested, the failure occurred under a load of 4680 lbs. Two delamination failures developed simultaneously in the specimen, both of them between the second and the third roving belts, as shown in Figure 43. Delamination A runs throughout the entire flexure, except for a small area near the end of the specimen, and is located along the lower surface of the second roving belt. Delamination B runs across a much smaller area at the end of the specimen, extending further along the edges of the flexure. It is located along the upper surface of the third roving belt.

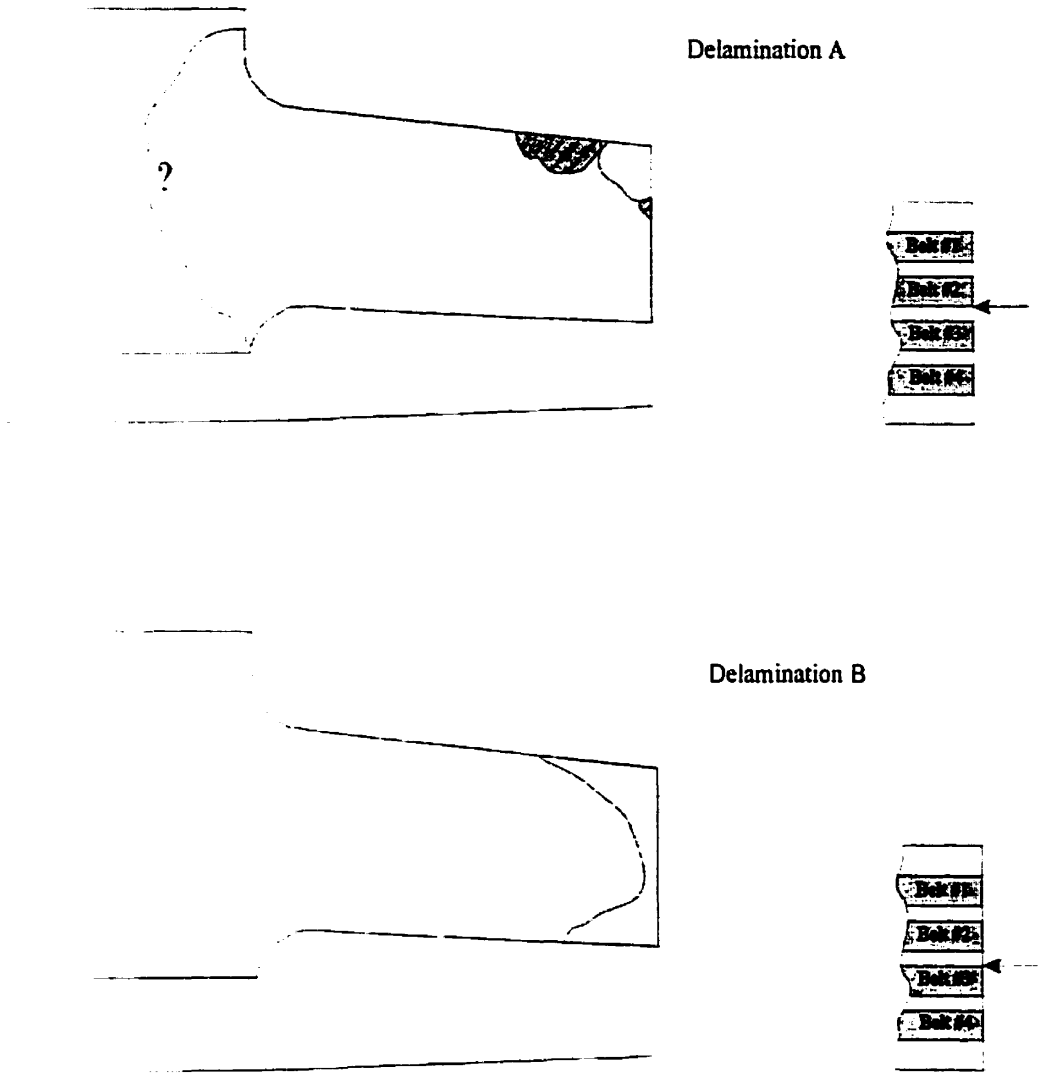

Figure 43 – Delamination failures observed for first specimen

For the second specimen tested under static load, the failure occurred under a load of 5025 lbs. As for the first specimen tested, two delaminations developed simultaneously near the mid-plane of the flexure. Delamination C extends over most of the flexure, except for a narrow band at the end of the flexure. It is located along the lower surface of the second roving belt. Delamination D runs along the upper surface of the third roving belt, across most of the flexure all the way to the end of the specimen. It extends further inboard on one side of the flexure.

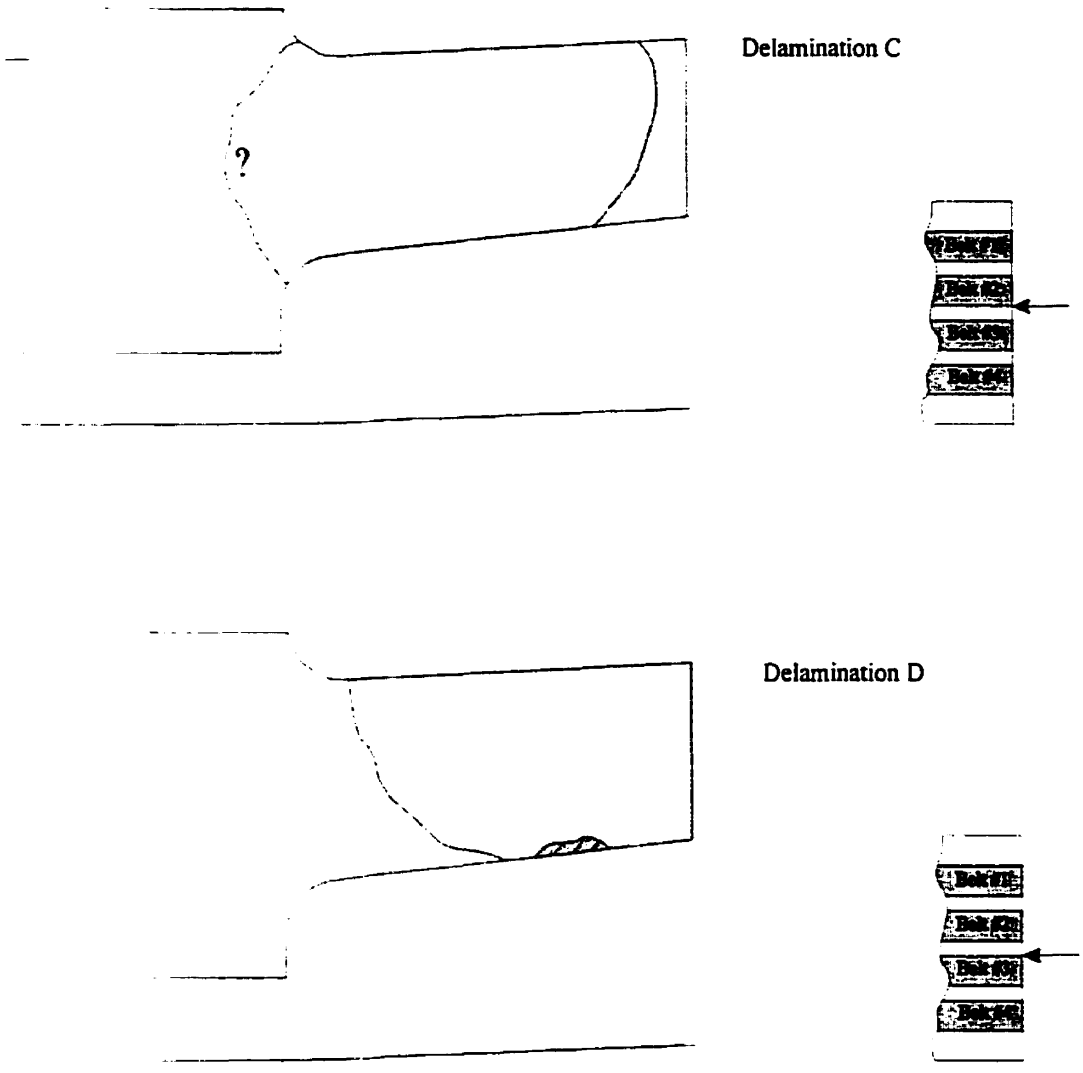

Figure 44 – Delamination failures observed for second specimen

Most of the delaminated surfaces in both specimens appear very smooth, indicating a clean separation of the fabric layers from the adjacent roving belt. However in certain small areas, indicated on Figure 43 and Figure 44 by a hatch pattern, the fabric plies between the two central roving belts were severely damaged.

Using the average of the failure loads for the two experiments performed, the ultimate load that can be carried by the specimen is determined to be 4850 lbs (21.5 kN).

Finite element calculations are then performed, with that ultimate load applied to the model.

Figure 45 shows an example of the interlaminar shear stress distribution in the specimen, at the interface located along the lower surface of the second roving belt. The highest interlaminar shear stresses are encountered at the edge of the specimen, close to the point where loads are applied. The interlaminar stress distribution is very similar for all ply locations through the thickness. Comparing these results with the characteristics of the delaminations obtained experimentally, it appears that the highest interlaminar shear stresses are encountered at the exact location where severe damage to the fabric plies was observed on the failed specimens. This suggests that in the present case, the interlaminar shear stresses are the principal factor driving the delamination failure.

Taking a closer look at this specific area, Figure 46 presents the variation of interlaminar shear stresses through the thickness of the model. The calculated interlaminar shear stresses are found to be the highest near the midplane of the flexure, between the second and the third roving belts. This indeed corresponds to the ply interface where delaminations were observed experimentally.

Further, interlaminar failure indices are calculated, for the interfaces where delaminations were observed experimentally, by applying a Maximum Stress failure criterion on the interlaminar shear stresses:

$$\text{F.I.} = \text{maximum of } \frac{\tau_{xz}}{S_h} \text{ and } \frac{\tau_{yz}}{S_h} \tag{27}$$

where S_h = interlaminar shear strength

Although this failure criterion is very simple, its use appeared appropriate in this case given the predominance of interlaminar stresses in delamination failure. Also, normal interlaminar stresses are not calculated by NASTRAN, therefore precluding the use of other failure criteria taking these stresses into account.

Because of the nature of the NASTRAN results files, it is not readily possible to transfer the failure indices to PATRAN, for postprocessing. A C++ program was therefore developed to transfer the required data and allow for a graphical postprocessing of the failure indices. The procedure used for the data transfer and the C++ code are described in Appendix B.

Figure 47 shows a plot of the interlaminar shear stress failure indices calculated for the interface located along the upper surface of the third roving belt. The maximum failure index, obtained along the edge of the specimen in the area where material splintering was observed experimentally, has a value of 1.45 .

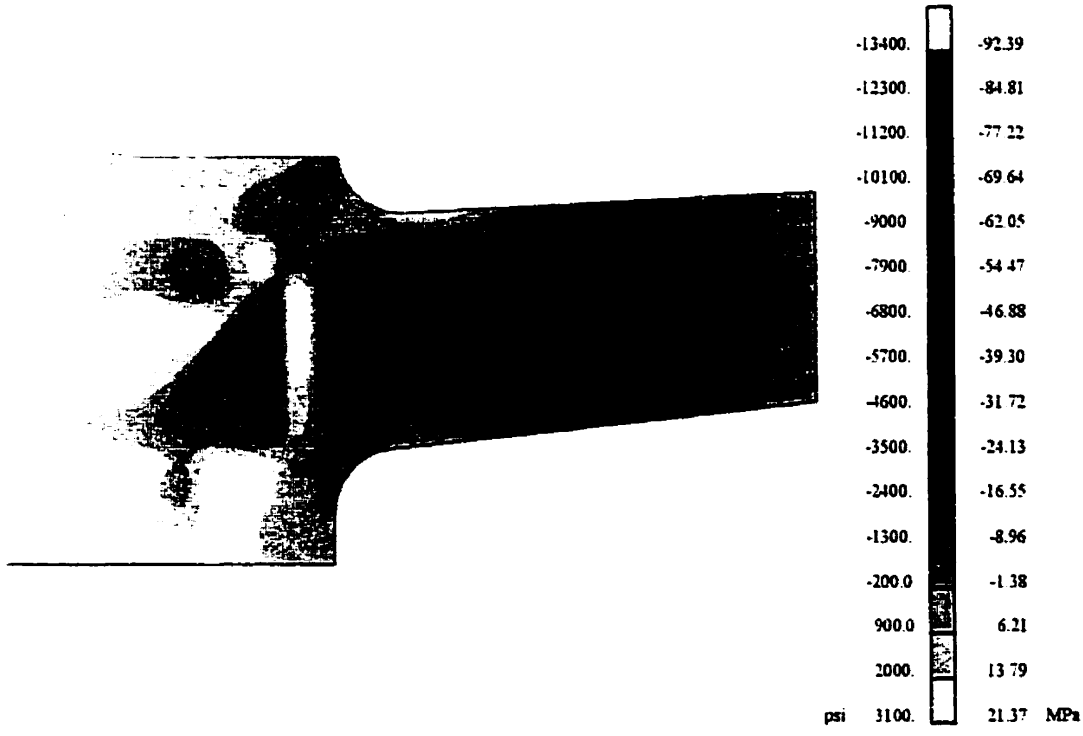

Figure 45 – Interlaminar shear stresses along the upper surface of the third roving belt. Applied load is 4850 lbs (21.5 kN).

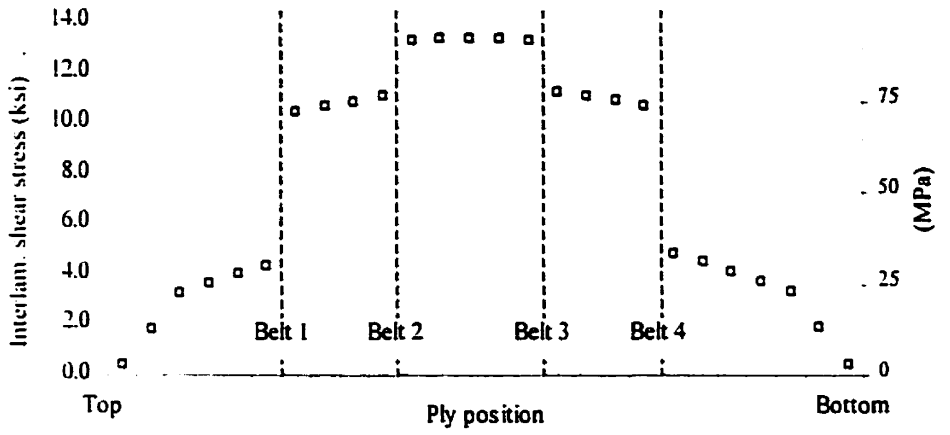

Figure 46 – Values of interlaminar shear stress at the ply interfaces, at location of maximum stresses. Applied load is 4850 lbs (21.5 kN).

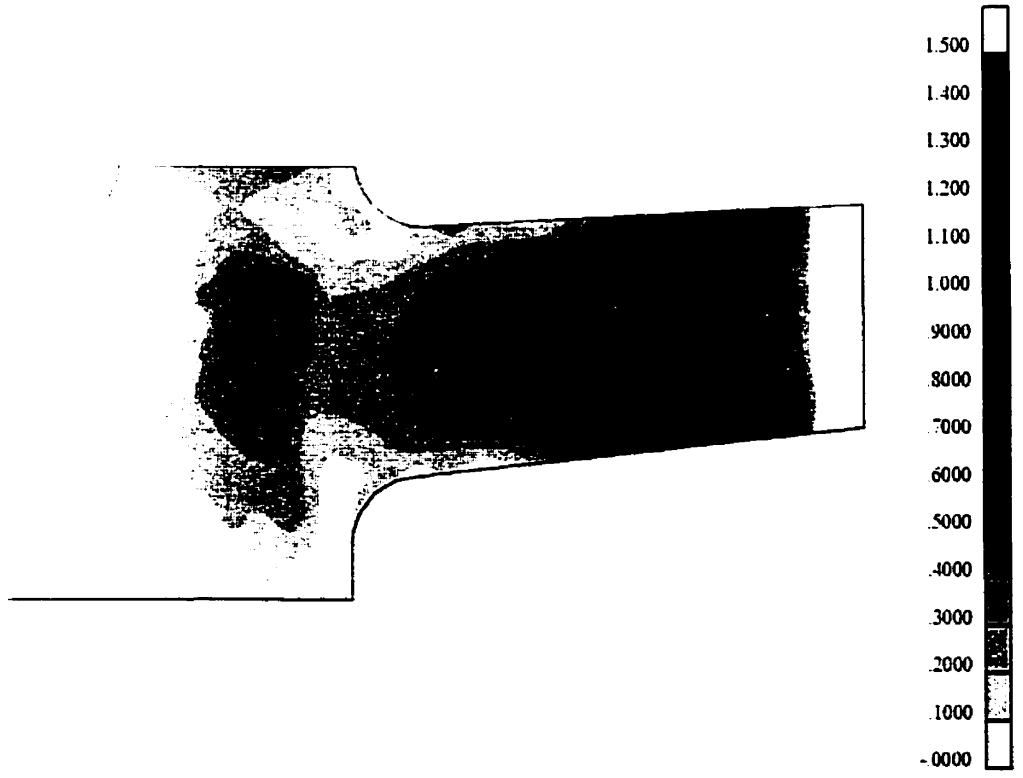

Figure 47 – Interlaminar shear failure indices (maximum stress) along the upper surface of the third roving belt. Applied load is 4850 lbs (21.5 kN).

The strength of the actual yoke specimens is therefore about 45% higher than predicted by the finite element model. However, the failure observed experimentally occurred exactly at the location where the maximum interlaminar shear stresses were predicted by the stress analysis.

It should be noted that the interlaminar failure predicted by the model does not necessarily correspond to catastrophic failure of the specimen. During the experiments, some initial matrix cracking, or small delaminations, may have occurred before the final catastrophic failure. Given the thickness and the size of the yoke specimen, it is very difficult to detect these early stages of damage leading to an extensive visible delamination.

Another important factor needs to be taken into account when comparing experimental results to the finite element model failure prediction. The value of interlaminar (out-of-plane) shear strength used in the analysis was determined using short-beam shear tests, in accordance with ASTM D-2344 standard. This method is widely used for material characterization. However, while it is well suited for quality control purposes, this method does not provide proper design data [36]. The interlaminar shear strength is determined using equations based on the homogeneous beam theory, which does not hold for short laminated beams. Therefore the calculations only provide an approximation of the actual interlaminar shear strength. In order to better characterize the interlaminar shear strength of the material, additional testing should be carried out using the double-notched specimen test method (ASTM D-2733 and D-3846).

5 *Fatigue experiments and analysis*

In Chapter 4, we described the characteristics of the test specimen and experimental setup used in the present study. A finite element model of the test specimen was developed, based on the model of the entire yoke. It was validated using the results of static tests performed on two specimens. The present chapter describes the fatigue loading experiments performed on yoke specimens. Experimental results are then correlated with the available material fatigue data, using the finite element model of the specimen and the Normalized Fatigue Life Model.

5.1 Experimental setup

The experimental setup used for testing yoke specimens under fatigue loading conditions is the same as the one used for static experiments (described in Section 4.3). However, difficulties were encountered when trying to apply oscillatory loads to the test specimen. Under both static or fatigue loading conditions, the loads required to cause failure of the specimen are quite high. Given the relatively low beamwise bending stiffness of the specimen, the moving head of the load frame is required to perform large strokes in order to generate these loads. Limitations in the stroke / load / frequency settings due to the hydraulics of the load frame had to be taken into account when selecting the test conditions.

Eight yoke specimens were subjected to cyclic loading. All the fatigue tests were performed with a load ratio R (maximum peak load divided by the minimum peak load) approximately equal to 0.5 . For each specimen, different percentages of the ultimate static failure load (selected as the maximum peak load) are applied in order to generate data points to build an S-N curve for the yoke specimens. The frequency of the oscillatory loads was set to 1 Hz.

5.2 Fatigue tests results

The first test specimen was subjected to cyclic loading with a peak load corresponding to 70% of the ultimate static failure load. The specimen failed by delamination after 10 072 load cycles. The failure is very similar in nature to what was observed for the two specimens subjected to static destructive tests (Section 4.7). Two delaminations developed simultaneously, both close to the midplane of the specimen. One delamination covers a small area at the ouboard end of the specimen, and is located along the upper surface of the third roving belt. The other delamination runs throughout the entire flexure, and is located along the lower surface of the second roving belt.

The second test specimen was subjected to cyclic loading with a peak load corresponding to 58% of the ultimate static failure load. The specimen completed over $1x10^6$ load cycles without showing any sign of failure. X-rays of the specimen taken after the test confirmed the absence of delamination. This test is considered to be a runout, i.e. nearly infinite fatigue life for the specimen under these loading conditions.

Test specimen #3 was subjected to cyclic loading with a peak load corresponding to 68% of the ultimate static failure load. The test was stopped after 382 100 load cycles, after small cracks were observed in the thin resin coat covering the edges of the specimen. However, X-rays of the specimen taken after the test did not indicate the presence of any delamination in the specimen.

Test specimen #4 was subjected to cyclic loading with a maximum load corresponding to 70% of the ultimate static load, as was done for the first test. The specimen completed 22 700 load cycles without any sign of failure, at which point the test was stopped. This specimen was then used for static tests.

Test specimen #5 was subjected to cyclic loading with a maximum load corresponding to 85% of the ultimate static failure load. The specimen failed by delamination after 27 750 load cycles. Multiple delaminations occurred simultaneously in

the specimen, all of them being located close to the midplane of the specimen, between the second and the third roving belt.

Test specimen #6 was subjected to cyclic loading with a maximum load corresponding to 80% of the static failure load. The specimen failed after 53 660 cycles, due to a component failure within the test fixture.

Test specimens #7 and #8 were subjected to cyclic loading with a maximum load corresponding to 80% and 88% of the ultimate static load, respectively. Specimen #7 failed by delamination after 113 910 load cycles, while specimen #8 failed after 9160 load cycles, again by delamination. Both specimens failed after friction caused some damage at the interface between the loading head and the surface of the specimen. The combination of high loads and small oscillatory motion between the two parts, during a long period of time, appeared to cause an overheating of the resin at the point of contact.

Table 7 presents a summary of the fatigue testing performed on yoke specimens. The ultimate static failure load (21.5 kN) was obtained by taking the average failure load for the two specimens failed under static conditions (Section 4.7).

Test ID	Max. peak load (kN)	% of ult. static failure load	Stress ratio	N_f (cycles)
1	15	70 %	0.55	10 072
2	12.5	58 %	0.54	1 003 370
3	14.6	68 %	0.51	382 100
4	15	70 %	0.57	22 700
5	18.3	85 %	0.51	27 750
6	17.2	80 %	0.49	53 660
7	17.2	80 %	0.51	113 910
8	19.0	89 %	0.47	9 160

Table 7 – Summary of fatigue experiments performed on yoke specimens

Specimen failures occurred suddenly, without prior visual or acoustic signs of damage (except for surface damages on specimens # 7 and 8). Also, for all of the experiments performed, the specimens exhibited no significant change in stiffness, even during the last few cycles before failure. Figure 48 shows an S-N plot of the fatigue test results. All the experiments were included in the plot for comparison purposes, even though some points do not correspond to failure of the specimen. The y-axis of the graph indicates the peak applied load, expressed as a percentage of the ultimate static failure load. There is obviously not enough data to establish a meaningful S-N curve for the yoke specimens. However, the test points appear to align in the shape of a standard fatigue (S-N) curve. i.e. decreasing fatigue life with increasing applied load.

Note on Figure 48 that early failure of yoke specimen #1 (which occurred after approximately $1x10^4$ load cycles) is inconsistent with the rest of the experimental results. This test specimen failed significantly earlier than expected.

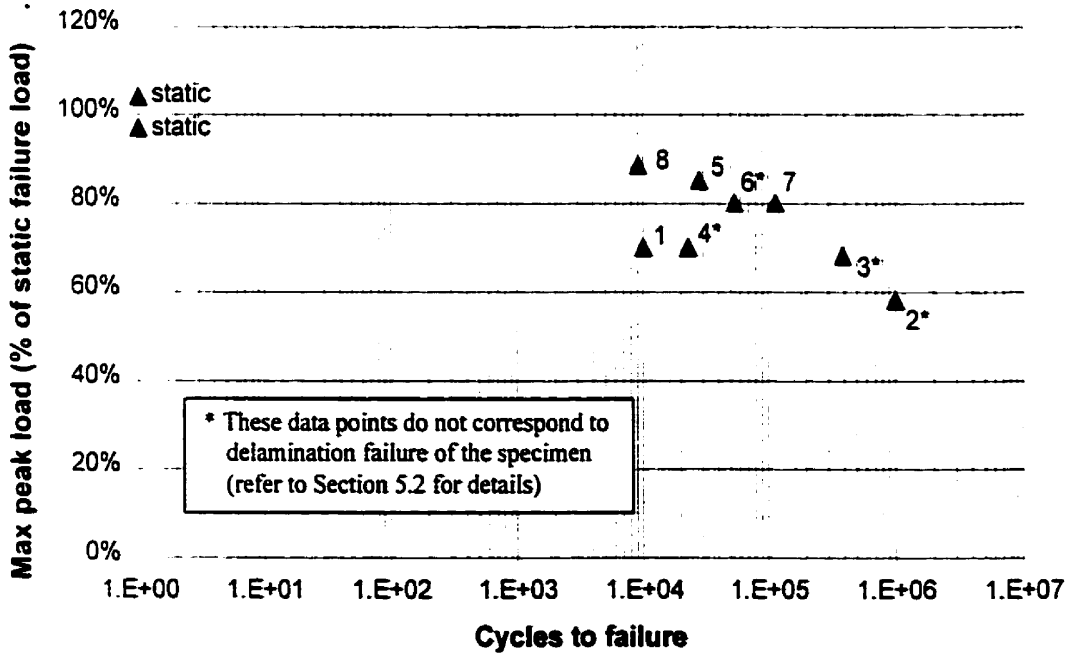

Figure 48 – S-N plot of the yoke specimen fatigue tests results

5.3 Material fatigue properties characterization

In order to analyze the current fatigue test results using the finite element model of the yoke specimen, the fatigue characteristics of the materials from which the yoke is built – fiberglass tape, roving and woven fabric – need to be evaluated. Similarly to the approach that was previously taken for static failure of the specimens, only the interlaminar shear component of the stress will be considered in the analysis. This was shown to yield satisfactory results in terms of delamination failure prediction.

Interlaminar shear fatigue data from material characterization tests is only available for the tape and roving plies [37]. A limited number of tests were performed. All material fatigue testing was done at the same level of mean stress, with different values of oscillatory stresses (or stress ratio) for each data point in order to generate an S-N curve. Fatigue testing of yoke specimens, on the other hand, was performed at a constant stress ratio, with different values of mean and oscillatory stresses for each data point. Yoke specimens fatigue data can therefore not be directly correlated with the material fatigue characterization data available. In order to establish a correlation between yoke specimen fatigue results and material fatigue data, a technique is required to collapse the two families of curves – constant mean stress and constant stress ratio – into a single general fatigue curve.

In a series of papers, Adam and Al. [38,39,40] proposed a method to convert all related fatigue life data for a given material into a single two parameters fatigue curve, regardless of the state of stress or the stress ratio. This will be referred to as the 'Normalized Fatigue Life Model'. First, non-dimensional stresses are calculated by dividing the mean stress (σ_m), alternating stress (σ_a) and the compressive strength (σ_c) by the tensile strength (σ_t):

$$\sigma_a = (\sigma_{max} - \sigma_{min})/2$$
$$\sigma_m = (\sigma_{max} + \sigma_{min})/2 \qquad (28)$$

$$q = \sigma_m / \sigma_t$$
$$a = \sigma_a / \sigma_t \qquad (29)$$
$$c = \sigma_c / \sigma_t$$

The following empirical relationship may then be derived, where f, A and B are curve fitting constants:

$$a = f[(1-q)(c+q)]^u = f[(1-q)(c+q)]^{A+B\log N_f} \qquad (30)$$

Note that there is a linear relationship between the parameter u – called the 'master curve life parameter' – and (log N_f). The constant f used for curve fitting is dependant on the material tested. By rearranging (30), the following equation can be obtained:

$$u = \frac{\ln(a/f)}{\ln[(1-q)(c+q)]} = A + B\log N_f \qquad (31)$$

The method described above was developed for carbon fibre reinforced composites, for tension/tension and tension/compression experimental fatigue data. Shokrieh [41] used the same model, again for carbon fibre composites, and extended it to shear fatigue loading conditions. For shear loads in (28) and (29), σ_m represents the mean shear stress. σ_a the alternating shear stress and σ_t the shear strength. Given that there is no difference between positive and negative shear strength ($\sigma_c = \sigma_t$), parameter 'c' in (31) is equal to unity for shear fatigue loading conditions. Shokrieh also determined, based on experimental data, that a better curve fitting was obtained by adding a (log $_{10}$) to the left hand side of (31). For shear fatigue loading conditions, the relationship is therefore as follows:

$$u = \log_{10}\left\{\frac{\ln(a/f)}{\ln[(1-q)(1+q)]}\right\} = A + B\log N_f \qquad (32)$$

In the present study, use of the Normalized Fatigue Life Model is extended to glass fiber reinforced composites. The method is first applied to the tape and roving interlaminar shear fatigue life data available. For each fatigue data point, the normalized stresses 'a' and 'q' are calculated, then the master curve life parameter 'u' is computed. It should be remembered that the value of 'f' in (32) is material dependant. Using the tape and roving interlaminar shear fatigue data only, the best linear correlation is obtained by setting f = 1.6 . The resultant (u) versus (log Nf) plot is shown in Figure 49. Note that the linear correlation of the data is extremely good. Also, the 'u' versus (log N_f) curves of the two materials. tape and roving, are very similar; this was to be expected since the fibers and resin are the same for both materials.

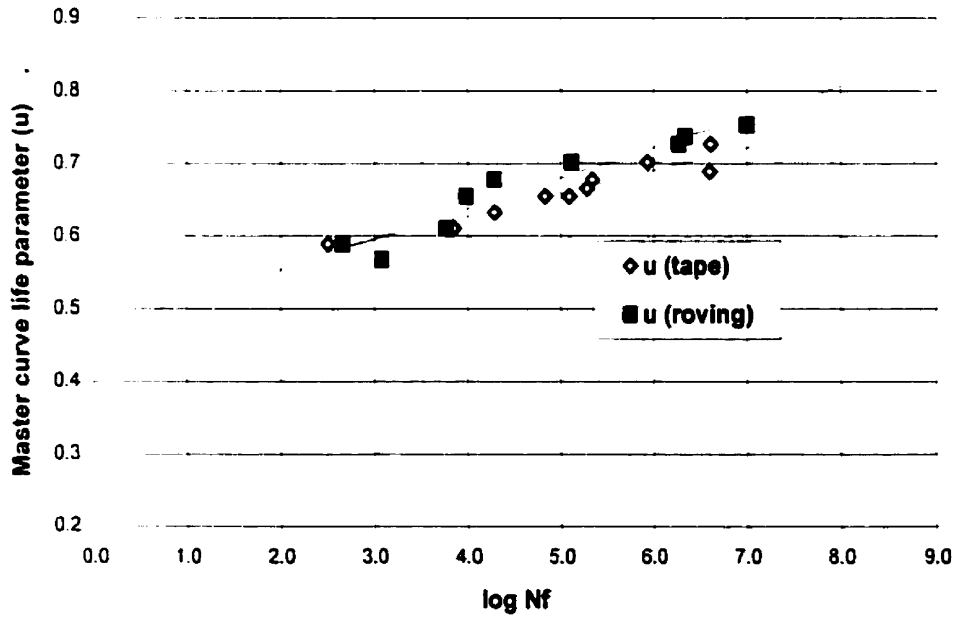

Figure 49 – Tape and roving interlaminar shear normalized fatigue life data (σ_{ult} = 9.18 ksi, f = 1.60)

Care should be taken however, in the interpretation of these results. The material coupon fatigue tests for both the tape and roving were all conducted using the same value of mean interlaminar stress (σ_m in (28)). The value of 'f' calculated based on this data might therefore not be representative of the material fatigue characteristics across a wider range of load levels. For further calculations, f = 1.60 will be used as a preliminary value for the yoke glass fiber material. This value will later be readjusted based on the results of the fatigue tests performed on yoke specimens (see Section 5.4).

No interlaminar shear fatigue life data is available for the woven fabric plies. The fiber and resin, however, are the same as for the tape and roving plies. Given that interlaminar shear failure involves mainly the shearing of the thin resin interlayer, it can reasonably be assumed that for an interlaminar shear fatigue failure, the behavior of fabric plies will be very similar to that of the tape and roving plies.

5.4 Prediction of yoke specimens fatigue life

In the previous section, interlaminar shear normalized fatigue life curves have been established for the glass fiber / epoxy materials used in the yoke. It is now desired to correlate these curves with the results of the fatigue experiments performed on yoke specimens. The location of the maximum interlaminar shear stresses, for loads applied to the outboard end of the specimen, was previously determined using the finite element model (Section 4.7). Again using the finite element model, the mean interlaminar shear stress (σ_m) and the oscillatory interlaminar shear stress (σ_a) are obtained for each one of the yoke specimen fatigue loading tests performed, for that specific location. Calculated values are shown in Table 8. Then using the normalized fatigue life model described in the previous section, the normalized stresses and the master curve life parameter 'u' are calculated for each one of the experiments. The value of interlaminar shear strength used in the computation of the normalized stresses 'q' and 'a' is obtained from material characterization data (σ_{ult} = 9.18 ksi). The resulting (u) versus (log N_f) plot is shown in Figure 50. along with the corresponding tape and roving normalized fatigue curves. It appears that hardly any correlation can be made between the two sets of data.

Test ID	Mean load		Mean stress, σ_m		Osc. load		Osc. stress, σ_a	
	(lbs)	(kN)	(psi)	(MPa)	(lbs)	(kN)	(psi)	(MPa)
1	2618	11.65	7780	53.6	753	3.35	2364	16.3
2	2157	9.60	6500	44.8	652	2.90	2053	14.2
3	2472	11.00	7379	50.9	809	3.60	2535	17.5
4	2641	11.75	7843	54.1	730	3.25	2293	15.8
5	3101	13.80	9081	62.5	1011	4.50	3150	21.7
6	2888	12.85	8512	58.7	978	4.35	3051	21.0
7	2910	12.95	8572	59.1	955	4.25	2981	20.6
8	3146	14.00	9200	63.4	1124	5.00	3492	24.1

Table 8 – Applied loads and corresponding interlaminar shear stresses (mean and oscillatory) for yoke specimen fatigue experiments

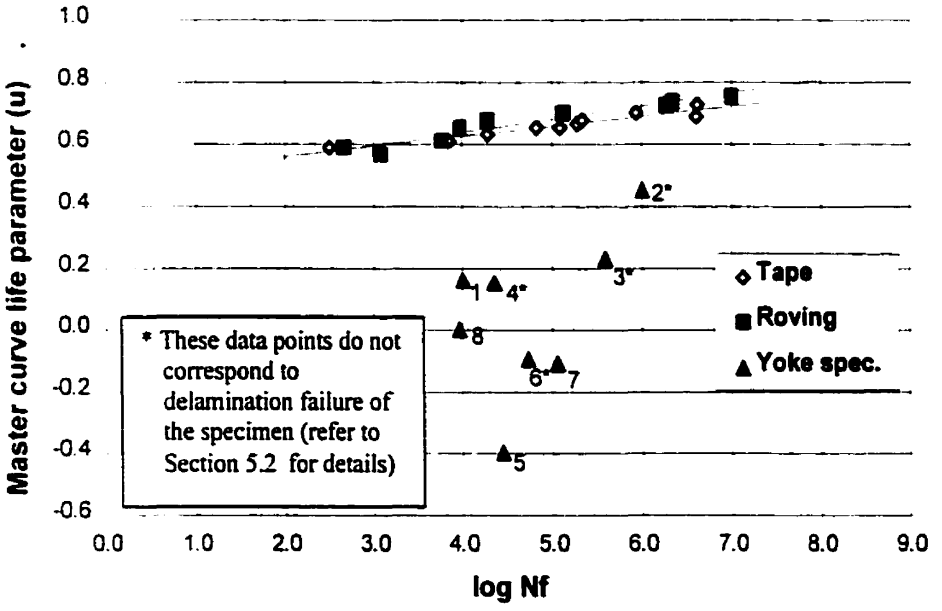

Figure 50 – Interlaminar shear normalized fatigue life data for yoke specimens fatigue experiments (σ_{ult} = 9.18 ksi, f = 1.60)

However, the value of interlaminar shear strength obtained from material characterization data ('theoretical' strength) differs significantly from the value of strength based on the static destructive tests of yoke specimens, and calculated with the finite element model (Section 4.7). For the maximum static load that the yoke test specimen can withstand (4850 lbs, 21.5 kN), the maximum interlaminar shear stress, as calculated with the finite element model is equal to 13.35 ksi, i.e. 45% above the 'theoretical' value of strength.

This error in the calculated stresses is inherent to the model, and will be considered as such in the calculations related to the specimen fatigue life. Therefore using 13.35 ksi as a 'corrected' value of interlaminar shear strength, the normalized stresses 'q' and 'a' are recalculated, and the master curve life parameter 'u' is computed for each one of the experiments. The resulting (u) versus (log N_f) plot is shown in Figure 51, along with the tape and roving normalized fatigue life curves. The use of a 'corrected' value of interlaminar shear strength yields to a better correlation between the yoke specimens fatigue test points and the material fatigue data.

As in the plots from previous results, all eight yoke specimen fatigue experiments are included in the graph. It should be remembered however, that only data points # 1, 5, 7 and 8 represent fatigue failure (delamination) of the corresponding test specimen. Failure of test specimen #1 showed to be inconsistent with the rest of the experimental data; therefore this data point will not be included in the calculations. Also, failure of specimens #7 and 8 occurred after the surface of the yoke in contact with the test fixture started to wear out due to friction. Comparing these two data points with the rest of the experimental results in Figure 48, it can reasonably be assumed that even without the surface damages, the specimens would have failed after approximately the same number of load cycles, and therefore that the surface damages had no significant influence on the fatigue failure.

Now, using test points # 5, 7 and 8 together with the tape and roving coupon fatigue data, the 'best fit' value for parameter 'f' in equation (32) is found to be equal to

0.56. This value should be more representative of the yoke fiberglass material than the preliminary value presented in section 5.3, given that it is based on data collected from experiments representing a wider range of fatigue loading conditons. Figure 52 shows the resulting (u) versus (log N_f) plot, along with the interlaminar shear normalized fatigue life curve which corresponds to the best linear fit of all the data points. Given that parameter 'f' has no physical meaning (it is merely a curve fitting constant) and that mathematically, its value is not restricted to a specific range, it is not possible to assess the validity of the 'f' value obtained here.

The same interlaminar shear fatigue life curve is shown in Figure 53, and compared with the test results from all yoke specimen fatigue tests. It is interesting to note that all the points on the plot not corresponding to fatigue failure of the specimen – namely test points #1, 2, 3, 4 and 6 – are located above the normalized fatigue life curve. This means that indeed, additional load cycles were (or should have been) required in order to cause failure of these specimens.

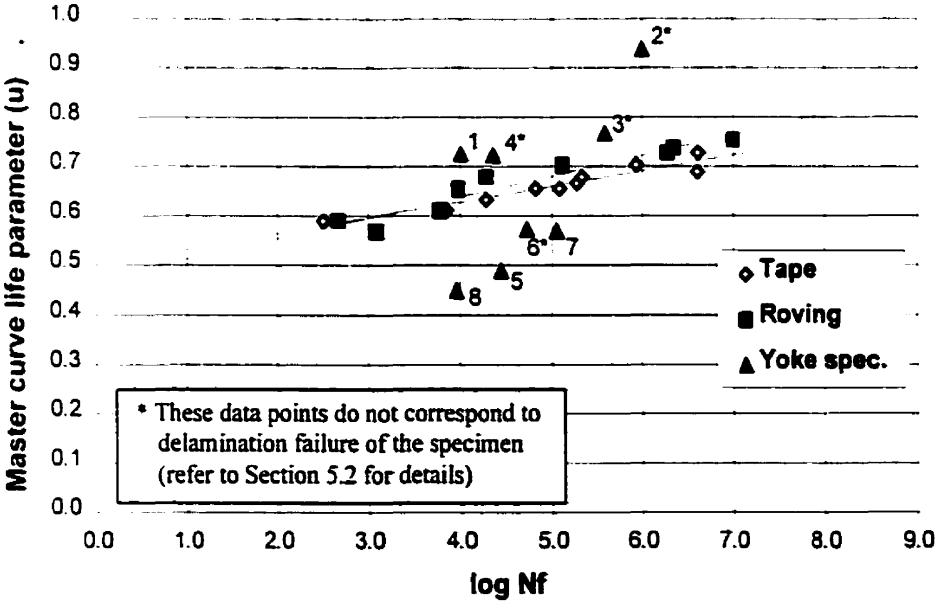

Figure 51 – Interlaminar shear normalized fatigue life data for yoke specimens fatigue experiments (σ_{ult} = 13.35 ksi, f = 1.60)

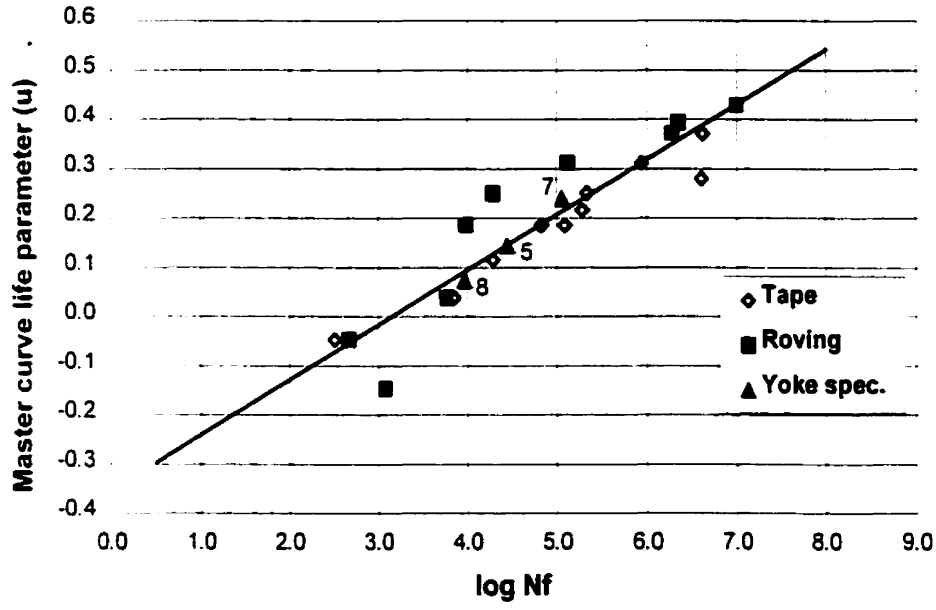

Figure 52 – Interlaminar shear normalized fatigue life curve for yoke fiberglass material (σ_{ult} = 13.35 ksi, f = 0.56)

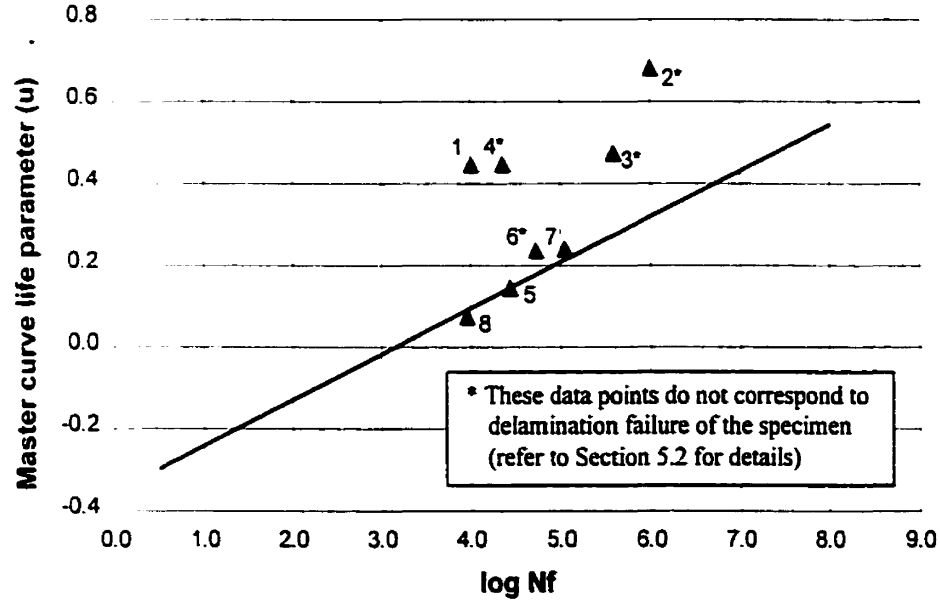

Figure 53 – Normalized fatigue life curve and yoke specimen experiments

The graph presented in Figure 52 can be used to predict the failure of laminated composites structures (made of the same material) under given fatigue loading conditions, using the Normalized Fatigue Life Method described in this chapter. The curve is believed to be reasonably representative of the yoke fiberglass material interlaminar shear fatigue characteristics, considering the limited amount of experimental data on which it is based: four specimens tested until delamination failure (among which one is highly questionable), one specimen failure due to a problem with the test fixture, and three fatigue tests interrupted prior to failure of the specimen. Obviously, additional fatigue tests performed at various mean and oscillatory stress levels would allow to determine more accurately these fatigue properties.

Finally note that within the scope of the present study, the normalized fatigue life curve was established using both material characterization data (material coupon fatigue testing) and fatigue experiments performed on yoke specimens. We can reasonably believe that a very similar curve would have been obtained if one was to use material coupon fatigue testing data only, provided that this data covers a wide range of mean and oscillatory interlaminar stress loading conditions. This is a primary motivation in actual applications of this method, such as in the design of complex laminated composite parts. It will allow to evaluate the fatigue properties of the complex laminated part based on readily available material fatigue characterization data, i.e. without having to manufacture and test specimens of the part.

6 *Conclusions*

6.1 Summary

The goal of the present research project was to develop an analytical method to predict the failure of a helicopter main rotor yoke, made of laminated fiberglass composite, under fatigue loading conditions. From a previous set of fatigue experiments, it is known that the primary failure mode of the main rotor yoke is delamination driven by interlaminar shear. A finite element model of the yoke was developed using a commercial finite element code, and validated against the available experimental data. A set of fatigue experiments were then performed on representative test specimens cut out of actual yokes. Results of these fatigue tests were correlated with the available material coupon fatigue data, using a finite element model of the specimen and the Normalized Fatigue Life model. From the analytical and experimental work performed, the following conclusions can be drawn:

- The 'dummy plies' technique was successfully used to avoid some difficulties inherent to modeling of tapered laminates.
- The finite element model adequately simulated the beamwise bending characteristics of the yoke flexure, but not its chordwise bending characteristics.
- For static tests performed on yoke specimens, the model was capable of accurately predicting the location of initial failure, but yielded about 50% error for the failure load prediction, based on the maximum stress criterion (interlaminar shear stresses).
- The Normalized Fatigue Life Model provided very good linear correlation for the yoke material (tape and roving) coupon fatigue data. This confirms that the method – initially developed for carbon fiber reinforced composites – can be readily extended to glass fiber / epoxy laminated composites.

- The Normalized Fatigue Life Model achieved a good correlation between the material coupon fatigue data and the yoke specimen fatigue test results.

6.2 Recommendations for future work

Further work would be required to improve the method and result in a tool that could readily be used for practical design applications. Some suggestions for future work on the subject are given below:

- Additional material fatigue tests are required to fully characterize the material properties. The fatigue properties of fiberglass fabric plies need to be characterized. Also, for the tape and roving unidirectional plies, fatigue data need to be obtained for a wider range of mean and oscillatory stresses.
- The apparent inadequacy of the finite element model to represent the chordwise bending characteristics of the yoke flexure should be investigated.
- Additional fatigue tests need to be performed on yoke specimens, at various load levels, in order to obtain a set of experimental results that is statistically more significant. It should also be considered to redesign the test fixture, in order to avoid some of the difficulties that were encountered in the present work (friction on the specimen, test fixture failure).
- Within the scope of this study, fatigue experiments and the corresponding analyses were only performed for yoke test specimens subjected to beamwise bending loads. The failure of yoke specimens under more complex loading conditions – including axial tension loads and chordwise oscillatory bending loads – needs to be investigated.
- In the present work, failure analyses (static and fatigue loading conditions) were based on the interlaminar shear stresses only. Although this yielded to a reasonably good agreement with the experimental data, the influence of other stress components should be included in order to obtain a better accuracy.

Appendix A

A simple cantilever beam test case (Figure 54), made of CQUAD4 shell elements, is used to verify the validity of the "dummy plies" technique. One half of the beam (near the clamped end) consists of an eight-ply laminate. Four of these plies terminate at mid-length, so that only four plies remain in the thinner half of the beam. Both normal and transverse bending loads are applied at the tip of the beam. The material properties and thickness of the individual plies are the same as in the actual yoke model.

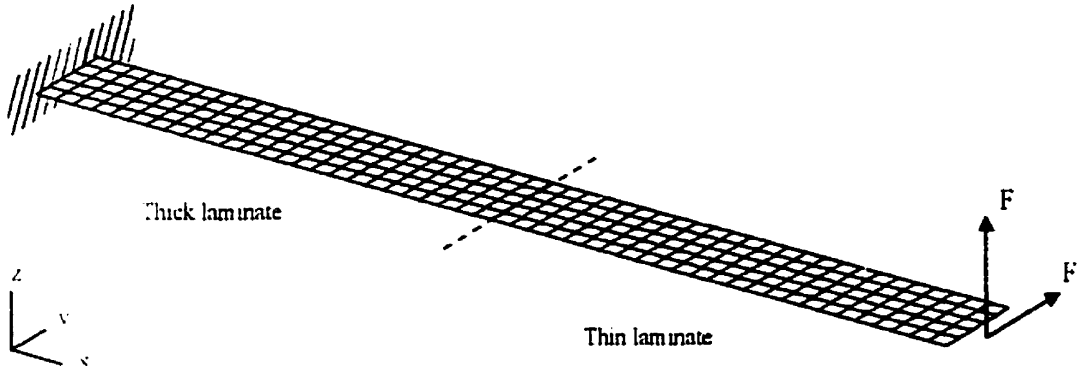

Figure 54 – Test case – cantilever beam model

Two different models were used for the analysis. In model A, the thin part of the laminate (after the ply drops) is made up of only four plies. In model B, all eight original plies are included in the thin section of the beam, but the thickness of the dropped plies is reduced to $1x10^{-15}$ inches (dummy plies). Details about the various laminates in models A and B are given in Table 9.

Examples of results obtained with the two different models are shown on the next pages. It clearly appears that the two models are equivalent in terms of calculated stress results, thus validating the "dummy plies" technique. Moreover, stress results calculated using the 'dummy plies' technique are shown to be more realistic, because it is continuous across the entire length of the ply. Displacement results (not shown) obtained with the two models are also identical.

Thick layup Model A & B			Thin layup			
			Model A		Model B	
ID	Thickness	Material	ID	Thickness	ID	Thickness
1	0.008	fabric	1	0.008	1	0.008
2	0.008	tape			2	$1x10^{-15}$
3	0.008	tape	2	0.008	3	0.008
4	0.008	fabric			4	$1x10^{-15}$
5	0.008	fabric			5	$1x10^{-15}$
6	0.008	tape	3	0.008	6	0.008
7	0.008	tape			7	$1x10^{-15}$
8	0.008	fabric	4	0.008	8	0.008

Table 9 – Characteristics of laminates in cantilever beam test case, model A and model B

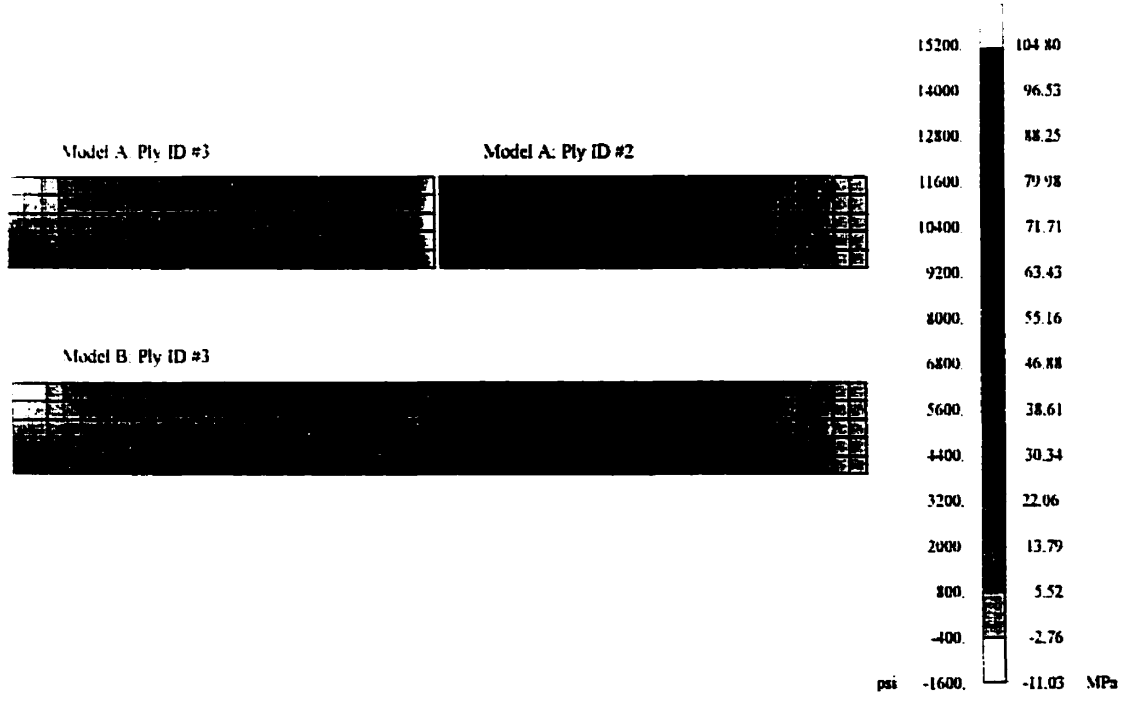

Figure 55 – Cantilever beam test case, Stress results (-xx component) in layer 3.

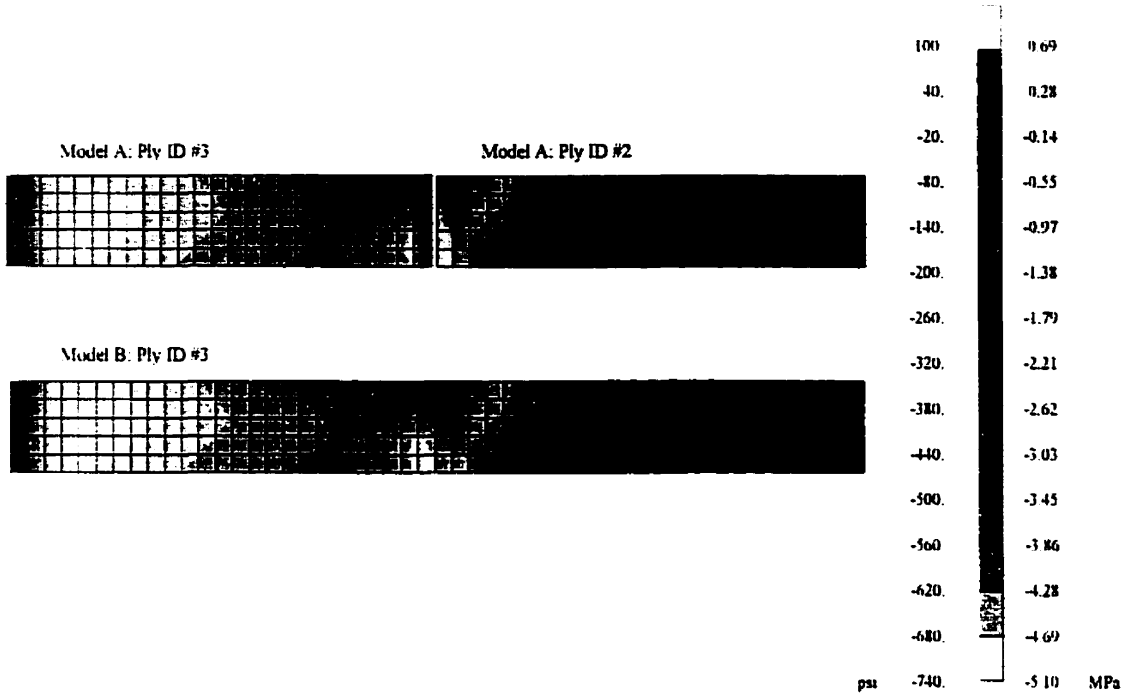

Figure 56 – Cantilever beam test case, Stress results (-xy component) in layer 3.

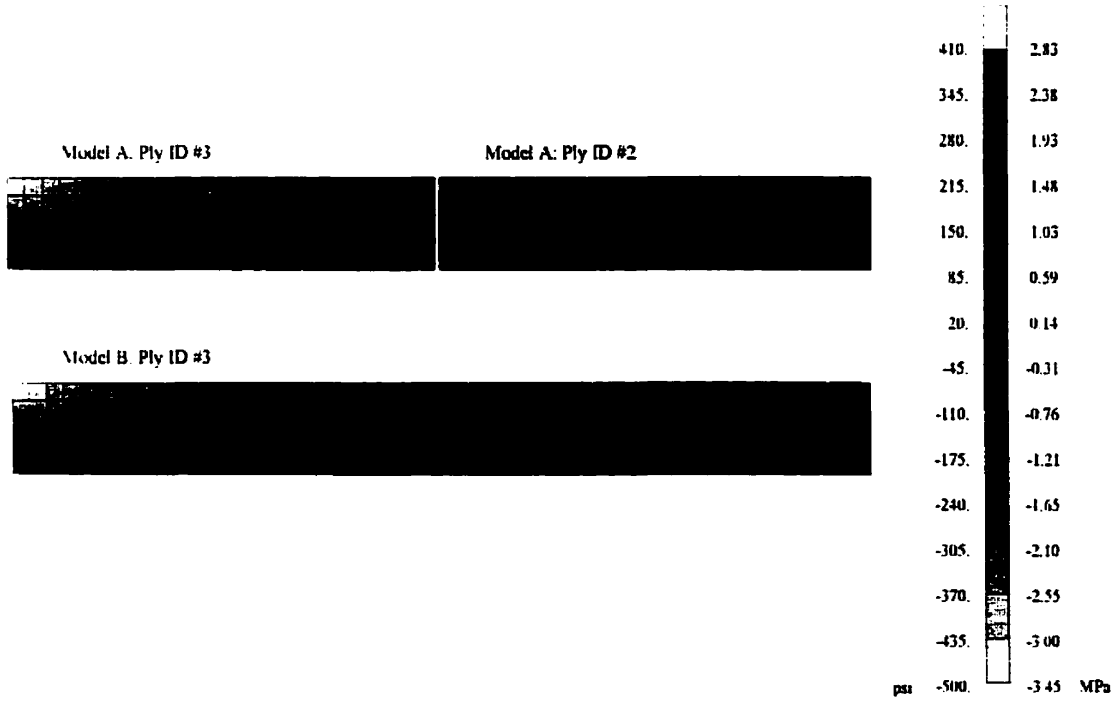

Figure 57 – Cantilever beam test case, Stress results (-xz component) in layer 3.

Appendix B

With the current version (V69) of NASTRAN, it is not possible to have composite failure indices written to the binary results output file (*.op2*), which is used to transfer results to PATRAN. The failure indices are only available in the text results file (*.f06*). The following procedure has been developed, to allow postprocessing of the failure indices in PATRAN.

First, a NASTRAN DMAP (Direct Matrix Abstraction Program) is used to redirect all the failure indices output into a new results file labeled '*.ndx*'. The DMAPs used for this purpose are as follows:

Linear statics (SOL 101):	*fail_index_lin.dmap*
Non-linear statics (SOL 106):	*fail_index_nl.dmap*

The C++ program *extract.C* is then used to read into the *.ndx* file, extract the failure indices for the selected composite layers. The utility generates both a PATRAN2.5 elements results file (*.els*) and the corresponding PATRAN2.5 Results template file (*.res_tmpl*). These are old file formats still supported by PATRAN. Details on the structure of these files can be found in [42]. The *.els* results file is finally read into PATRAN using the Import utility.

The two NASTRAN DMAPs *fail_index_lin.dmap* and *fail_index_nl.dmap* , and the C++ program *extract.C* are given in the following pages.

fail_index.dmap

```
$ This DMAP alter writes the composite element failure indices
$ to a user defined file rather than the conventional f06 output
$ file. Fortran unit 13 is used to write the failure indices.
$ The user needs to provide an ASSIGN statement such as:
$
$ assign userfile='{filename}' status=new unit=13 formatted delete
$
compile sedrcvr
alter 'OFP      OES1C,OEFIT','' $
type parm,,i,n,linespp $
linespp=getsys(linespp,9) $
paraml  kelm//'trailer'/1/s,n,noelem $ No. of nl elem. in model
noelem=20*noelem $ calc. lines per page to 20 x no. of elem.
putsys(noelem,9) $ set lines per page
putsys(13,2) $   write printed output to unit 13
ofp      oefit//s,n,cardno $
putsys(linespp,9) $ reset lines per page to original value
putsys(6,2) $ restore unit 6 for printed output
ofp      oes1c//s,n,cardno $ ply stress output
endalter $
```

fail_index_new.dmap

```
$ The DMAP alter writes the composite element failure indices
$ to a user defined file rather than the conventional f06 output
$ file.  Fortran unit 13 is used to write the failure indices.
$ The user needs to provide an ASSIGN statement such as:
$
$ assign userfile='{filename}' status=new unit=13 formatted delete
$
$ The failure indices are dependent on the value of the parameter
$ LGDISP.  For a LGDISP of -1, subDMAP SEDRCVR writes the failure
$ indices to the OEFIT data block.  If LGDISP is 1, subDMAP NLSTATIC
$ writes the indices to the OEFIT data block.
$
compile sedrcvr
alter 'OFP      OES1C,OEFIT','' $
type parm,,i,n,linespp $
linespp=getsys(linespp,9) $
paraml  kelm//'trailer'/1/s,n,noelem $ No. of nl elem. in model
noelem=20*noelem $ calc. lines per page to 20 x no. of elem.
putsys(noelem,9) $ set lines per page
putsys(13,2) $   write printed output to unit 13
ofp      oefit//s,n,cardno $
putsys(linespp,9) $ reset lines per page to original value
putsys(6,2) $ restore unit 6 for printed output
ofp      oes1c//s,n,cardno $ ply stress output
endalter $
$
$
compile nlstatic
alter 'OFP     OESCP,OEFIT','' $
type parm,,i,n,linespp $
linespp=getsys(linespp,9) $
paraml  kelm//'trailer'/1/s,n,noelem $ No. of nl elem. in model
noelem=20*noelem $ calc. lines per page to 20 x no. of elem.
putsys(noelem,9) $ set lines per page
putsys(13,2) $   write printed output to unit 13
ofp      oefit//s,n,cardno $
putsys(linespp,9) $ reset lines per page to original value
putsys(6,2) $ restore unit 6 for printed output
ofp      oescp//s,n,cardno $ ply stress output
endalter $
```

extract.C

```
#include <stdio.h>
#include <iostream.h>
#include <iomanip.h>
#include <fstream.h>
#include <string.h>
#include <stddef.h>
#include <ctype.h>

int write_header(char *, char *, char *);
int write_template();
int process_lines(char *);
int write_res(int, int, float *);

ifstream infile;
ofstream outfile;
ofstream templfile;
int n_results;          // Number of requested results
int result_id[10];      // Ply ID for requested results

int main(void)
{

char ndxfile[80], elsfile[80], restmplfile[80];
char title[40], subtitle[40];
char line[256];

cout << "Input file (without the .ndx extension):  ";
cin >> ndxfile;
cout << "How many results to process? (max = 6)  ";
cin >> n_results;

for (int i=0; i<n_results; i++)
      {
      cout << "Ply ID for result #" << i+1 << " :  ";
      cin >> result_id[i];
      }

strcpy(elsfile,ndxfile);
strcpy(restmplfile,ndxfile);
strncat(elsfile,".els",4);
strncat(ndxfile,".ndx",4);
strncat(restmplfile,".res_tmpl",9);

infile.open(ndxfile);
if(!infile) {
      cout << "Cannot open .ndx file.\n";
      return 1;
      }
```

```
outfile.open(elsfile);
if(!outfile) {
      cout << "Cannot open .els file.\n";
      return 1;
      }

templfile.open(restmplfile);
if(!templfile) {
      cout << "Cannot open .res_tmpl file.\n";
      return 1;
      }

infile.getline(line,255,'\n');
strncpy(title,line+5,39);

infile.getline(line,255,'\n');
strncpy(subtitle,line+6,39);

write_header(ndxfile, title, subtitle);

write_template();

process_lines(subtitle);

infile.close();
outfile.close();
templfile.close();

cout << "Job finished. \n";

return 0;
}



int process_lines(char *subtitle)
{
char cur_line[256];
static int elm_type;
static int elm_id = 0;
static float index[10];
static int j = 0;
int ply_id;

while(!infile.eof())
{

infile.getline(cur_line,255,'\n');

if (strstr(cur_line,"PAGE") != NULL) continue;
if (strstr(cur_line,subtitle) != NULL) continue;
```

```
if (strstr(cur_line,"SUBCASE") != NULL) continue;
if (strstr(cur_line,"STEP") != NULL) continue;
if (strstr(cur_line,"ELEMENT") != NULL) continue;
if (strstr(cur_line,"ID") != NULL) continue;

if (strstr(cur_line,"F A I L U R E") != NULL)
      {
      if (strstr(cur_line,"Q U A D 4") != NULL) elm_type = 4;
      else if (strstr(cur_line,"T R I A 3") != NULL) elm_type = 3;
      continue;
      }

if (strstr(cur_line,"TSAI-WU") != NULL)
      {
      if (elm_id != 0)
            write_res(elm_id, elm_type, index);
      sscanf(cur_line," %d",&elm_id);
      ply_id = 1;
      j = 0;
      continue;
      }

if (isdigit(cur_line[25]) != 0)              // Ply ID...
      {
      sscanf(cur_line," %d",&ply_id);
      continue;
      }

else if (result_id[j] == ply_id)             // Interlaminar index...
      {
      sscanf(cur_line," %f",&index[j]);
      j++;
      continue;
      }

}          // End of while loop

return 0;
}



int write_res(int id, int type, float *indices)
{
outfile << "\n";

outfile << setiosflags(ios::right) << setw(8) << id;
outfile << setiosflags(ios::right) << setw(8) << type << endl;

for (int i=0; i<n_results; i++)
      outfile << setiosflags(ios::right) << setw(13) << indices[i];
```

```
return 0;
}


int write_header(char *file, char *title, char *subtitle)
{
int i = 1;

outfile << subtitle << "\n";
outfile << setiosflags(ios::right) << setw(5) << n_results << endl;
outfile << "From file '" << file << "'\n";

while (title[i] != '\0')
      {
      if (isalpha(title[i]) != 0)
            title[i] = tolower(title[i]);
      i++;
      }
outfile << title;

return 0;
}


int write_template()
{
templfile << "KEYLOC = 0" << "\n\n";

for (int i=0; i<n_results; i++)
      {
      templfile << "TYPE = SCALAR" << "\n";
      templfile << "COLUMN = " << i + 1 << "\n";
      templfile << "PRI = Index" << "\n";
      templfile << "SEC = Interlam " << result_id[i] << "-" <<
result_id[i] + 1 << "\n\n";
      }

return 0;
}
```

References

1. Valisetty, R.R., Rehfield, L.W., *A new ply model for interlaminar stress analysis*, ASTM: Delamination and Debonding of Materials, STP 876, 1985, pp.52-68

2. Pipes, R.B., Pagano, N.J., *Interlaminar stresses in Composite Laminates under uniaxial extension*, Journal of Composite Materials, V4, 1970, pp.538-548

3. Wang, A.S.D., Crossman, F.W., *Some New Results on the Edge effect in Symmetric Composite Laminates*, Journal of Composite Materials, V11, 1977, pp.92-106

4. Raju, I.S., Crews, J.H., *Interlaminar Stress Singularities at a Straight Free Edge in Composite Laminates*, Computers and Structures, V14 #1-2, 1981, pp.21-28

5. Kim, R.Y., Soni, S.R., *Experimental and Analytical Studies on the Onset of Delamination in Laminated Composites*, Journal of Composite Materials, V18, 1984, pp.70-80

6. Soni, S.R., Kim, R.Y., *Delamination of Composite Laminates Stimulated by Interlaminar Shear*, ASTM: Composite Materials, Testing and Design, STP 893, 1986, pp.286-307

7. Pagano, N.J., Soni, S.R., *Global-Local Laminate Variational Model*, International Journal of Solids and Structures, V19 #3, 1983, pp.207-228

8. Whitney, J.M., Nuismer, R.J., *Stress Fracture Criteria for Laminated Composites containing Stress Concentrations*, Journal of Composite Materials, V8, 1974, pp.253-265

9. Kim, R.Y., Soni, S.R., *Failure of Composite Laminates due to Combined Interlaminar Normal and Shear Stresses*, Composites '86: Recent Advances in Japan and the United States, 1986, Japan Society for Composite Materials, pp.341-350

10. Brewer, J.C., Lagace, P.A., *Quadratic Stress Criterion for Initiation of Delamination*, Journal of Composite Materials, V22 #12, 1988, pp.1141-1155

11. Kassapoglou, C., Lagace, P. A., *An Efficient Method for the Calculation of Interlaminar Stresses in Composite Materials*, Journal of Applied Mechanics, V53 #12, 1986, pp.744-750

12. Fish, J.C., Lee, S.W., *Strength of Glass-Epoxy Laminates Based on Interply Resin Failure*, Proceedings American Society for Composites, 3rd Technical Conference, 1988, pp.242-252

13. Chan, W.S., Rehfield, L.W., O'Brien, T.K., *Analysis, Prediction, and Prevention of Edge Delamination in Rotor System Structures*, Journal of the American Helicopter Society, V36 #2, 1991, pp.44-51

14. Armanios, E.A., Rehfield, L.W., *Interlaminar Fracture Analysis of composite laminates under bending and combined bending and extension*, ASTM: Composite Materials, Testing and Design, STP 972, 1988, pp.81-94

15. Chan, W.S., Ochoa, O.O., *Delamination characterization of laminates under tension, bending and torsion loads*, Computational mechanics, V6 #5-6, 1990, pp.393-405

16. Fish, J.C., *Stress Analysis of Composite Rotor Systems*, Proceedings AHS 47th Annual Forum, 1991, pp.615-627

17. Kemp, B.L., Johnson, E.R., *Response and Failure Analysis of a Graphite-Epoxy Laminate Containing Terminating Internal Plies*, Collection of Technical Papers (AIAA) - AIAA/ASME/ASCE/AHS Structures, Structural Dynamics & Materials Conference, Part 1, 1985, pp.13-21

18. Curry, J.M., Johnson, E.R., Starnes, J.H., *Effect of Dropped Plies on the Strength of Graphite-Epoxy Laminates*, Collection of Technical Papers (AIAA) - AIAA/ASME/ASCE/AHS Structures, Structural Dynamics & Materials Conference, 1987, pp.737-745

19. Hashin, Z., *Failure Criteria for Unidirectional Fiber Composites*, Journal of Applied Mechanics, V47, 1980, pp.329-334

20. Hoa, S.V., Daoust, J., Du, B.L., *Interlaminar Stresses in Tapered Laminates*, Polymer Composites, V9 #5, 1988, pp.337-344

21. Hoa, S.V., Daoust, J., *Parameters Affecting Interlaminar Stresses in Tapered Laminates Under Static Loading Condition*, Polymer Composites, V10 #5, 1989, pp.374-383

22. Fish, J.C., Lee, S.W., *Delamination of Tapered Composite Structures*, Engineering Fracture Mechanics, V34 #1, 1989, pp.43-54

23. Fish, J.C., Lee, S.W., *Edge Effects in Tapered Composite Structures*, Proceedings AHS National Technical Specialist's Meeting on Advanced Rotrcraft Structures, , 1988. pp.1-16

24. Vizzini, A.J., Lee, S.W., , Damage Analysis of Composite Tapered Beams, Journal of the American Helicopter Society, V40 #2, 1995, pp.43-49

25. Salpekar, S.A., Raju, I.S., O'Brien, T.K., *Strain-Energy-Release Rate Analysis of Delamination in a Tapered Laminate Subjected to Tension Load*, Proceedings American Society for Composites, 3rd Technical Conference, 1988, pp.642-654

26. Armanios, E.A., Parnas, L., *Delamination analysis of tapered laminated composites under tensile loading*, ASTM: Composite Materials, Fatigue and Fracture, STP 1110, 1991, pp.340-358

27. Murri, G.B., Salpekar, S.A., O'Brien, T.K., *Fatigue Delamination Onset Prediction in Unidirectional Tapered Laminates*, ASTM: Composite Materials, Fatigue and Fracture, STP 1110, 1991, pp.312-339

28. Murri, G.B., O'Brien, T.K., Salpekar, S.A., *Tension Fatige of Glass-Epoxy and Graphite-Epoxy Tapered Laminates*, Journal of the American Helicopter Society, V38 #1, 1993, pp.29-37

29. O'Brien, T.K., *Generic Aspects of Delamination in Fatigue of Composite Materials*, Journal of the American Helicopter Society, V32 #1, 1987, pp.13-18

30. Murri, G.B., Rousseau, C.Q., *Fatige Life Methodology for Tapered Composite Flexbeam Laminates*, Proceedings AHS 53rd Annual Forum, 1997, pp.20-32

31. *MSC/NASTRAN V68 Reference Manual*, MacNeal-Schwendler Corporation.

32. Whitney, J.M., *Structural Analysis of Laminated Anisotropic Plates*, Technomic Publishing Co., 1987.

33. Bell Helicopter Textron, Drawing no. 407-010-102

34. 407-010-101-105 Main Rotor Yoke S/N A-234 and A-237 Calibration Deflection Data, Bell Helicopter Structural Test Laboratory

35. Bell Helicopter Textron, Report no. 406-998-003

36. Mallick, P.K., *Fiber-Reinforced Composites – Materials Manufacturing and Design*, 2nd edition, Marcel Dekker Inc, New York, 1993, pp. 243-244.

37. Bell Helicopter Textron, Report no. 299-100-569

38. Adam, T., Fernando, G., Dickson, R.F., Reiter, H., Harris, B., *Fatigue Life Prediction for Hybrid Composites*, International Journal of Fatigue, V11 #4, 1989, pp.233-237

39. Gathercole, N., Adam, T., Harris, B., Reiter, H., *An Unified Model for Fatigue Life Prediction of Carbon Fibre / Resin Composites*, Proceedings of the 5th European Conference on Composite Materials, 1992, pp.89-94

40. Adam, T., Gathercole, N., Reiter, H., Harris, B., *Fatigue Life Prediction for Carbon Fibre Composites*, Advanced Composites Letters, V1, 1992, pp.23-26

41. Shokrieh, M.M., *Progressive Fatigue Damage Modeling of Composite Materials*, Ph.D. Thesis, Department of Mechanical Engineering, McGill University, Canada, 1996

42. MSC/PATRAN User's Manual, section 2.2 and 11.5